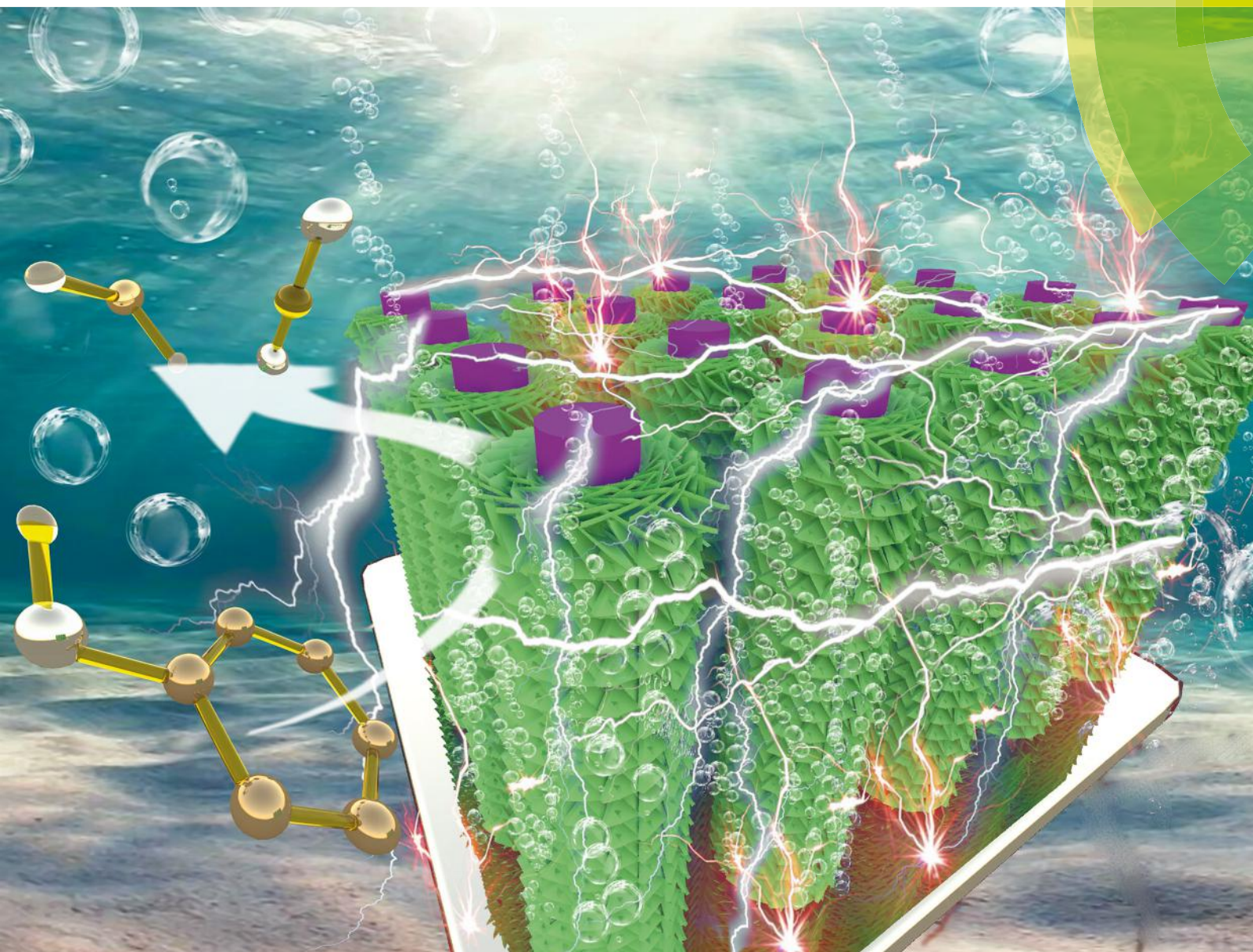# NJC

New Journal of Chemistry

rsc.li/njc

A journal for new directions in chemistry

ROYAL SOCIETY OF CHEMISTRY | Celebrating IYPT 2019

PAPER
Jin-Ming Wu *et al.*
TiO2 nanotrees for the photocatalytic and
photoelectrocatalytic phenol degradation

CNRS

![Royal Society of Chemistry logo]

Are you **passionate** about **chemistry** and **teaching**?

Or, do you know someone who is?

We are offering 130 Teacher Training Scholarships, in partnership with the Department for Education, to people starting chemistry teacher training in September 2019.

Find out more and check your eligibility at **rsc.li/scholarships**

New Journal of Chemistry
Impact factor: **3.069** | Issues per year: **48**

‹ View all journals

Recent	Issues	Collections

Previous Latest Next

New Journal of Chemistry

48 items

Cover info and contents

Editorial

Selenium & tellurium chemistry at the beginning of the 3rd millennium: a celebration of ICCST

Vito Lippolis and Claudio Santi

Vito Lippolis and Claudio Santi introduce the *New Journal of Chemistry* themed collection on selenium & tellurium chemistry at the beginning of the 3rd millennium: a celebration of ICCST.
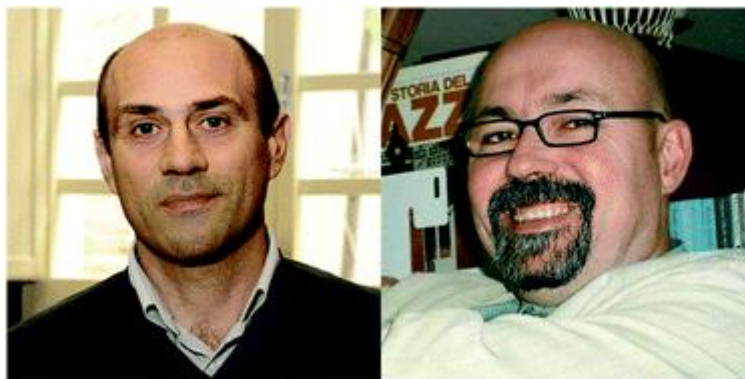
Download PDF   Article HTML

Perspective

Pyridyl and pyrimidyl chalcogenolates of coinage metals and their utility as molecular precursors for the preparation of metal chalcogenides

Vimal K. Jain

Synthesis of and metallophilic interactions in N-heterocyclic chalcogenolates of coinage metals have been described and their utility as molecular precursors for binary and ternary chalcogenide materials has been demonstrated.
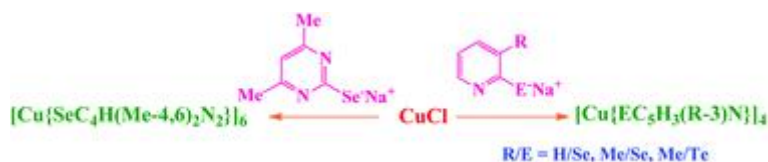
Mild and efficient rhodium-catalyzed deoxygenation of ketones to alkanes

Gilles Argouarch

Chlorodicarbonylrhodium(I) dimer: a simple catalyst for the reduction of carbonyl compounds also.

Download PDF   Article HTML

Substrate-switched dual functionalization of alkenes: catalyst-free synthetic route for β-hydroxy and β-keto thioethers

Satpal Singh Badsara, Pratibha Singh, Rakhee Choudhary, Rekha Bai and Mahesh C. Sharma

A substrate-controlled dual functionalization of alkenes under catalyst-free and solvent-free conditions to provide β-hydroxy thioethers and β-keto thioethers is described.

TiO$_2$ nanotrees for the photocatalytic and photoelectrocatalytic phenol degradation

Juan Xie, Wei Wen, Qi Jin, Xiao-Bo Xiang and Jin-Ming Wu

Constructing nanotrees is an effective method to enhance the photoelectrocatalytic efficiency of TiO$_2$ using single-crystalline trunks with an appropriate length.
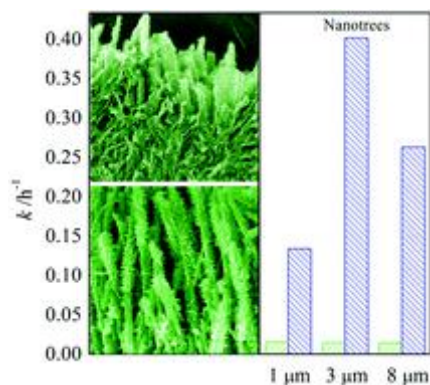
From the themed collection: [New Journal of Chemistry HOT Articles](#)

Download PDF   Article HTML

Influence of the channel size of isostructural 3d–4f MOFs on the catalytic aerobic oxidation of cycloalkenes

Patricio Cancino, Luis Santibañez, Christian Stevens, Pablo Fuentealba, Nathalie Audebrand, Daniel Aravena, Julia Torres, Sebastian Martinez, Carlos Kremer and Evgenia Spodine

The present work reports a new group of heterogeneous catalysts with a 3D structure, CuLnIDA, {[Cu$_3$Ln$_2$(IDA)$_6$]·8H$_2$O} (Ln: La^{III}, Gd^{III} or Yb^{III}), with an organic linker (H$_2$IDA: iminodiacetic acid).

The article was first published on 11 Jun 2019
New J. Chem., 2019, **43**, 11057-11064

Download PDF   Article HTML

Paper

Potassium *tert*-butoxide mediated aerobic hydroxylation of arylboronic acids: an application towards the synthesis of (*E*)-phenoxy acrylates

Ibrahim Muhammad, Madasamy Hari Balakrishnan, Manickam Sasidharan and Subramaniyan Mannathan

The first example of potassium *tert*-butoxide mediated aerobic hydroxylation of arylboronic acids affording phenols is described.
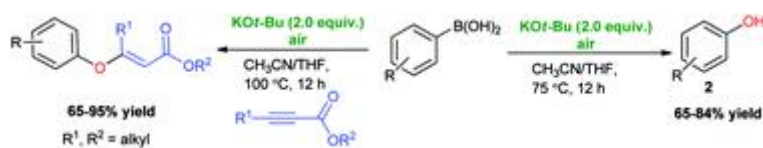
The article was first published on 12 Jun 2019
New J. Chem., 2019, **43**, 11065-11068

Download PDF   Article HTML

Paper

Room temperature trimethylamine sensing studies of mixed oxide VO_2–TiO_2 thin films deposited using the reactive dc magnetron co-sputtering technique.
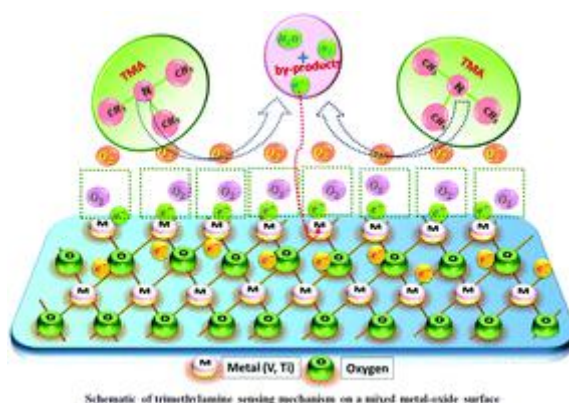
Schematic of trimethylamine sensing mechanism on a mixed metal-oxide surface

Download PDF   Article HTML

Paper

Synthesis of magnetic nanoflower immobilized lipase and its continuous catalytic application

Weifan Ren, Yao Li, Jihui Wang, Lin Li, Longquan Xu, Yuxuan Wu, Yi Wang, Xu Fei and Jing Tian

We have synthesized a kind of magnetic lipase–$Cu_3(PO_4)_2$ nanoflowers (lipase@MNFs), which can be separated quickly from the reaction system under the external magnetic field. Compared with free lipase, the lipase@MNFs exhibited higher enzymatic activity (~110%) and stability.

Top   Info   Search
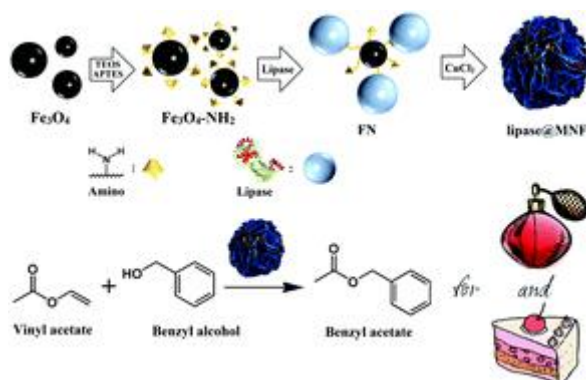
Paper

Synthesis of alkynyltellurides mediated by K₃PO₄ and DMSO

Manoela do Sacramento, Larissa Menezes, Bruna Goldani, Gelson Perin, Marcio S. Silva, Thiago Barcellos and Diego Alves

The reaction of diorganyl ditellurides with terminal alkynes is described using K_3PO_4 as a catalyst.
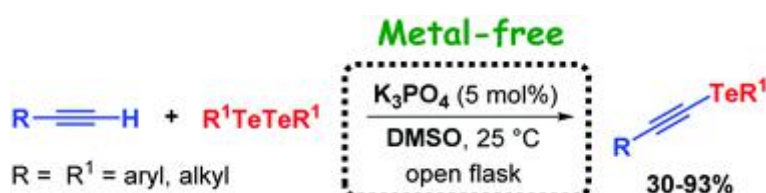
Paper

Effect of carbon-skeleton isomerism on the dielectric properties and proton conduction of organic cocrystal compounds assembled from 1,2,4,5-benzenetetracarboxylic acid and piperazine derivatives

Xiaoqiang Liang, Yixiang Chen, Li Wang, Feng Zhang, Zenglu Fan, Tingting Cao, Yaya Cao, Huifang Zhu, Xinyue He, Bolin Deng, Yazhi You, Yu Dong and Yamei Zhao

Two isostructural 2D supramolecular cocrystal compounds show different dielectric responses and proton conductivities due to the alteration of the carbon-skeleton of piperazine derivatives.

Download PDF   Article HTML

Paper

Synthesis, characterization and computational study of an ilmenite-structured $Ni_3Mn_3Ti_6O_{18}$ thin film photoanode for solar water splitting

Khadija Munawar, Fouzia Perveen, Muhammad Mehmood Shahid, Wan Jeffrey Basirun, Misni Bin Misran and Muhammad Mazhar

Thin films of a $Ni_3Mn_3Ti_6O_{18}$ solid solution photoanode have been deposited on an FTO coated glass substrate and experimental results are supported by DFT studies.

Download PDF   Article HTML

Paper

Substituent effects on the stability, physicochemical properties and chemical reactivity of nitroimidazole derivatives with potential antiparasitic effect: a computational study

Linda Campos-Fernández, Carolina Barrientos-Salcedo, Edtson E. Herrera Valencia, Rocío Ortiz-Muñiz and Catalina Soriano-Correa
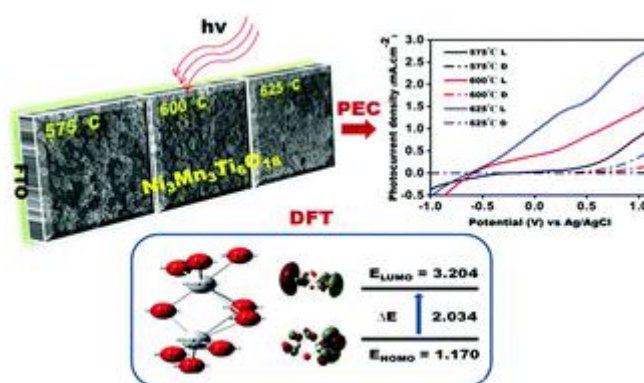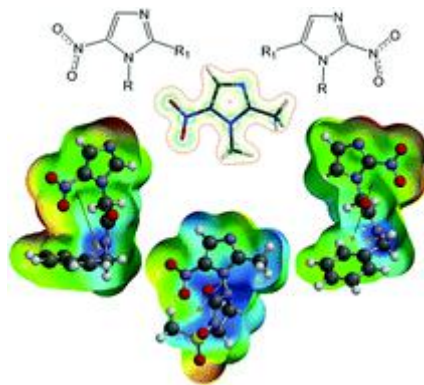
The article was first published on 10 Jun 2019

Download PDF   Article HTML

Paper

Ni–Fe hybrid nanocubes: an efficient electrocatalyst for non-enzymatic glucose sensing with a wide detection range

Cancan Bao, Qiangqiang Niu, Xiaowei Cao, Chang Liu, Hui Wang and Wenbo Lu

A sensor for the determination of glucose is developed based on Ni–Fe hybrid nanocubes, which exhibit excellent sensing performance.
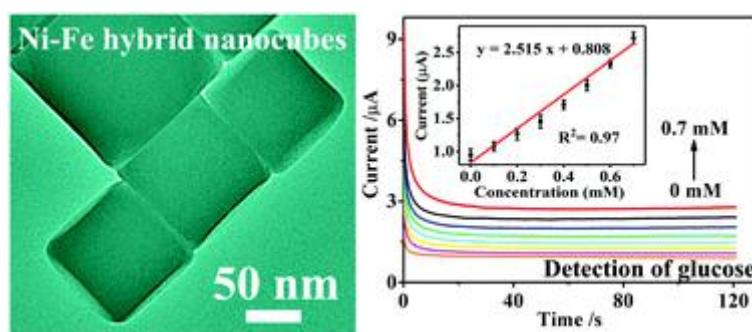
The article was first published on 13 Jun 2019

Download PDF   Article HTML

A simple strategy based on a highly fluorinated polymer blended with a fluorinated polymer containing phosphonic acid to improve the properties of PEMFCs

Etienne Labalme, Ghislain David, Pierrick Buvat and Janick Bigarre

Phosphonic acid containing fluorinated blend membranes led to new PEMFCs with a proton conductivity of 40 mS cm^{-1} at 80 °C.
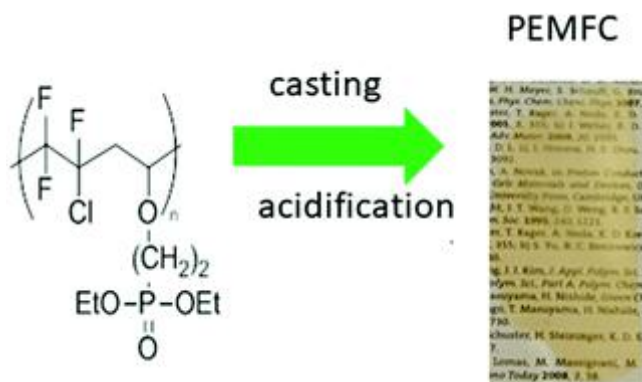
The article was first published on 14 Jun 2019
New J. Chem., 2019, **43**, 11141-11147

Download PDF   Article HTML

Facile charge transfer in fibrous PdPt bimetallic nanocube counter electrodes

Muhamad Adam Ramli, Siti Khatijah Md Saad, Elvy Rahmi Mawarnis, Marjoni Imamora Ali Umar, P. Susthitha Menon, Mohd Yusri Abd Rahman and Akrajas Ali Umar

Enhanced charge transfer is realized in DSSCs that utilize poriferous PdPt bimetallic nanocubes as the counter electrode.
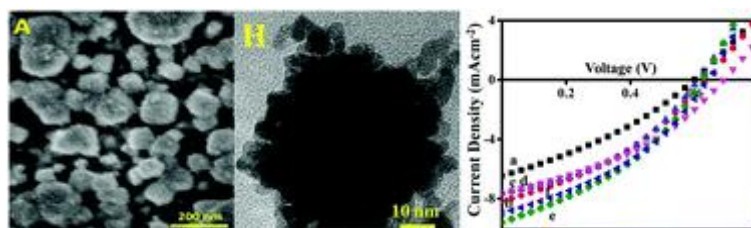
Paper

Synthesis of high-performance insensitive energetic materials based on nitropyrazole and 1,2,4-triazole

Minxian Xu, Guangbin Cheng, Hualin Xiong, Bohan Wang, Xuehai Ju and Hongwei Yang

A new family of symmetric nitropyrazole and 1,2,4-triazole derivatives and its energetic salts were obtained. The positive effect of ternary hydrogen bonds improve the performances of target compounds.
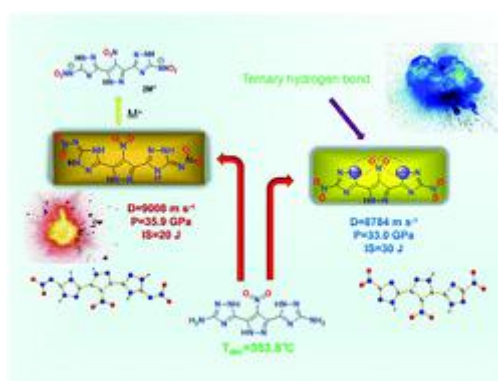
The article was first published on 14 Jun 2019
New J. Chem., 2019, **43**, 11157-11163

Paper

General microemulsion synthesis of organic–inorganic hybrid hollow mesoporous silica spheres with enlarged pore size

Yangyi Sun, Chengyu Zhang, Yijing Mao, Dongyu Pan, Dongming Qi and Ningyu Di

General microemulsion synthesis of organic–inorganic hybrid hollow mesoporous silica spheres with enlarge pore size with different kinds of pore expanders.
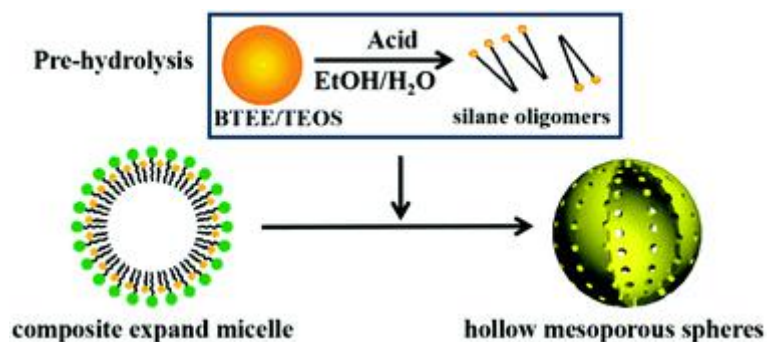
The article was first published on 13 Jun 2019

Download PDF   Article HTML

Paper

Phytic acid-based copper(II) ion-selective electrode on graphene oxide for potentiometric immunoassay of breast cancer antigen 15-3

Min Zheng, Yong-Jin Cao, Wei-Hua Cai, Xi Shi, Mou-Feng Wang and Yu-Jie Deng

A potentiometric immunoassay based on a copper(II) ion-selective electrode (Cu-ISE) was designed for the quantitative determination of carbohydrate antigen 15-3 (CA 15-3; a tumor marker associated with breast cancer).
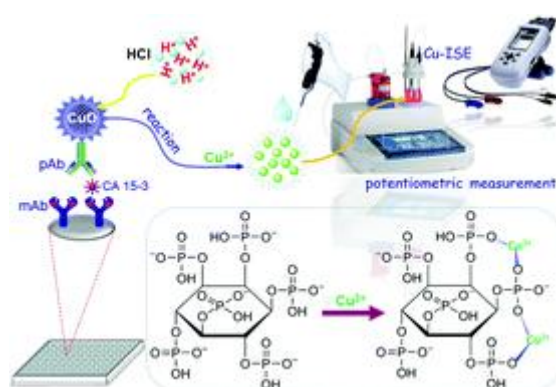
The article was first published on 18 Jun 2019

Hydroxypropyl β-cyclodextrin cross-linked multiwalled carbon nanotube-based chiral nanocomposite electrochemical sensors for the discrimination of multichiral drug atorvastatin isomers

Sharad S. Upadhyay and Ashwini K. Srivastava

Drugs having multiple chiral centres pose a greater risk to the human health as their pharmacological effects on human organs, cells and systems due to more number of enantiomers as compared to that of a single enantiomeric drug.
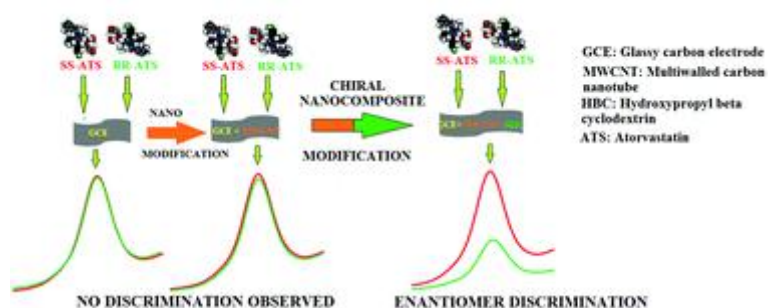
Download PDF   Article HTML

New methodology of nucleophilic substitution at three different centers of a seleniranium intermediate in reactions of 2-bromomethyl-1,3-thiaselenole with mercapto benzazoles

Svetlana V. Amosova, Andrey S. Filippov, Nataliya A. Makhaeva, Alexander I. Albanov and Vladimir A. Potapov

Regio- and stereoselective reactions accompanied by rearrangements with ring extension or contraction.

From the themed collection: Selenium & Tellurium chemistry at the beginning of the 3rd millennium:

Download PDF   Article HTML

Paper

Tracking pereirine and flavopereirine in pau-pereira using Raman and SERS spectroscopies

Lenize F. Maia, Márcia R. Almeida, Dhieniffer F. Carvalho, Nathália M. P. Rosa, Antonio Carlos Sant'Ana, Luiz Antônio S. Costa, Vanessa End de Oliveira, Angelo C. Pinto and Luiz Fernando C. de Oliveira

Raman and SERS spectroscopies have been used to identify the bioactive compounds pereirine and flavopereirine from stem bark, ethanolic crude extracts and infusions.

Download PDF   Article HTML

Paper

Solution and solid behavior of mono and binuclear zinc(II) and nickel(II) complexes with dithiocarbazates: X-ray analysis, mass spectrometry and cytotoxicity against cancer cell lines

Cássia de Q. O. Cavalcante, Daniel da S. Arcanjo, Guilherme G. da Silva, Diêgo M. de Oliveira and Claudia C. Gatto

We report the synthesis and characterization of metal complexes with dithiocarbazates and the cytotoxicity against the breast cancer line MDA-MB-231.

Paper

The role of a weakly coordinating thioether group in ligation controlled molecular self-assemblies and their inter-conversions in Ni(II) complexes of L-methionine derived ligand

Rakesh Kumar, Vishal Mutreja, Gyaneshwar Sharma, Sanjeev Kumar, Anzar Ali, S. K. Mehta, P. Venugopalan, Ramesh Kataria and Subash Chandra Sahoo

A series of Ni(II) complexes of an amino acid derived ligand (Salmet) has been synthesized, and characterized by various techniques including X-ray crystallography. Alkali ions K^+/Na^+ direct the conversion of monomers to multi-nuclear complexes.
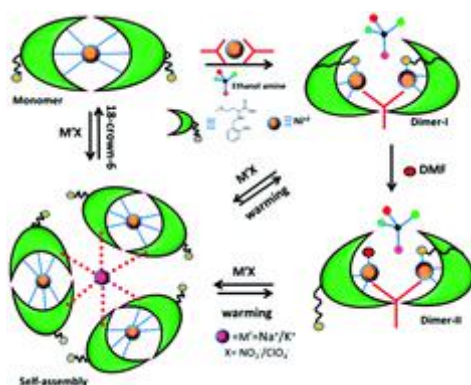
Download PDF   Article HTML

Paper

New flexible molecular probes bearing dansyl and TEMPO moieties for host–guest interactions in solution and gels

Sorin Mocanu, Iulia Matei, Anca Leonties, Victorita Tecuceanu, Anamaria Hanganu, Zamfirica Minea, Alina Stancu, Elena Irina Popescu and Gabriela Ionita

Host–guest interactions in functionalised alginate gels are evidenced by EPR and fluorescence spectra.
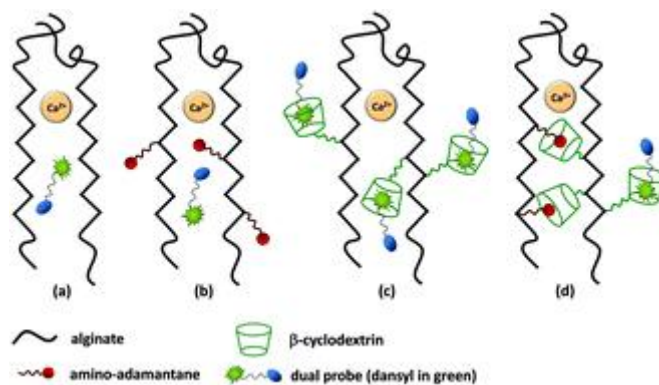
The article was first published on 27 Jun 2019

Download PDF   Article HTML

Paper

Further studies on the photoreactivities of ruthenium–nitrosyl complexes with terpyridyl ligands

Isabelle Sasaki, Silvia Amabilino, Sonia Mallet-Ladeira, Marine Tassé, Alix Sournia-Saquet, Pascal G. Lacroix and Isabelle Malfant

Exposure of the ruthenium terpyridyl complex to NO gas leads to the ruthenium–NO complex with nitrosation of the ligand.

The article was first published on 21 Jun 2019

Download PDF   Article HTML

Cycloaddition reactions on epitaxial graphene

Pablo A. Denis, C. Pereyra Huelmo and Federico Iribarne

By means of first principles calculations we studied the occurrence of cycloaddition reactions on the buffer layer of silicon carbide. Interestingly, the presence of the substrate favors the 1,3 cycloaddition instead of the [2+2] or [4+2] ones.
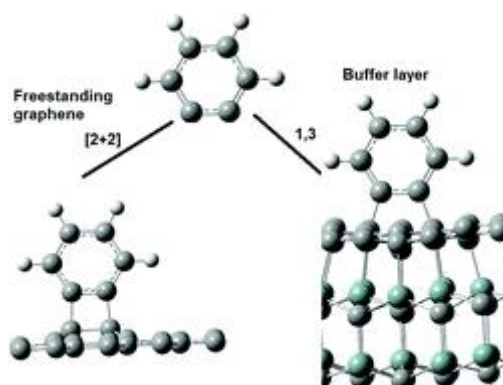
The article was first published on 19 Jun 2019
New J. Chem., 2019, **43**, 11251-11257
https://doi.org/10.1039/C9NJ02528F

Download PDF   Article HTML

Assessing the influence of phosphine substituents on the catalytic properties of self-stabilised digold(I) complexes with supporting ferrocene phosphinonitrile ligands

Ondřej Bárta, Ivana Císařová, Jiří Schulz and Petr Štěpnička

Dimeric Au(I) complexes with phosphinonitrile ligands remain highly catalytically active at low catalyst loadings thanks to self-stabilisation by dimerisation.
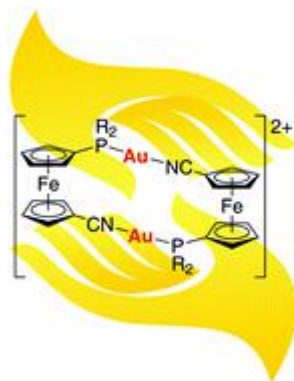
The article was first published on 21 Jun 2019

New J. Chem., 2019, **43**, 11258-11262

https://doi.org/10.1039/C9NJ02555C

Download PDF   Article HTML

Paper

Redox-triggered switch based on platinum(II) acetylacetonate complexes bearing an isomeric donor–acceptor conjugation ligand shows a high second-order nonlinear optical response

Yuan Zhang, Hongqiang Wang, Jinting Ye and Yongqing Qiu

Pt(II) acetylcetonate complexes with an isomeric D–A ligand exhibiting exceptionally large hyperpolarizabilities are promising redox-triggered NLO switches.
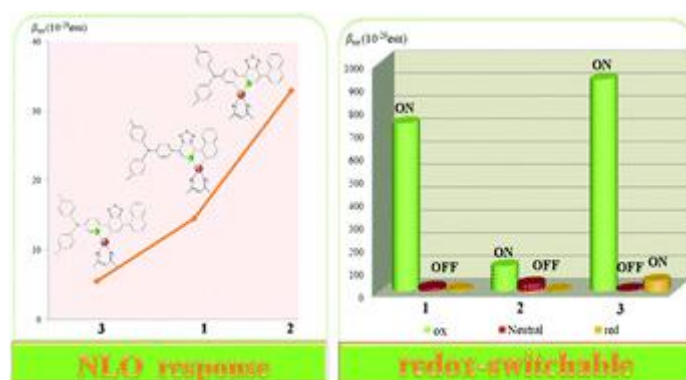
The article was first published on 18 Jun 2019

New J. Chem., 2019, **43**, 11263-11274

https://doi.org/10.1039/C9NJ02183C

Top   Info   Search

Carbon dioxide utilization in the efficient synthesis of carbamates by deep eutectic solvents (DES) as green and attractive solvent/catalyst systems

Iman Dindarloo Inaloo and Sahar Majnooni

Deep eutectic solvents as a green solvent/catalyst system for directly synthesizing carbamates from amines, CO_2 and alkyl halides.

Download PDF   Article HTML

Carbon/TiO$_2$/Fe$_2$O$_3$ hybrid shells as efficient visible light photocatalysts

Minggui Wang, Jie Han, Ganyin Yuan and Rong Guo

Mesoporous $C/TiO_2/Fe_2O_3$ hollow hybrids with TiO_2/Fe_2O_3 p–n heterojunctions and electrically conductive carbon show high photocatalytic performance.
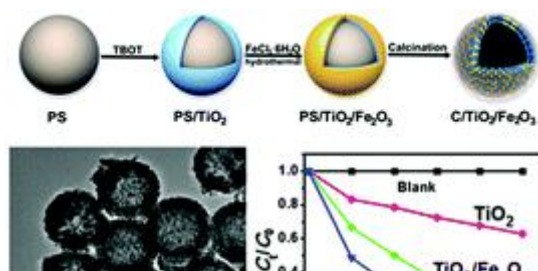
Download PDF   Article HTML

Paper

Comparative evaluation of ^{99m}Tc-MBIP-X/^{11}[C] MBMP for visualization of 18 kDa translocator protein

Pooja Srivastava, Neelam Kumari, Dipti Kakkar, Ankur Kaul, Pravir Kumar and Anjani K. Tiwari

An elevated translocator protein (18 kDa, TSPO) density is observed during inflammation in the brain and peripheral organs making it a viable target for imaging.
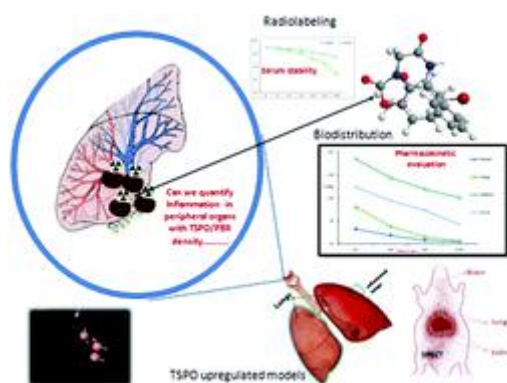
Download PDF   Article HTML

Paper

Induction of transferrin aggregation by indazolium [tetrachlorobis(1*H*-indazole)ruthenate(III)] (KP1019) and its biological function

Klaudyna Śpiewak, Sylwia Świątek, Barbara Jachimska and Małgorzata Brindell

Pre-incubation of **KP1019** with transferrin leads to the formation of adducts/aggregates, which inhibit the cytotoxic properties of **KP1019**.

The article was first published on 21 Jun 2019
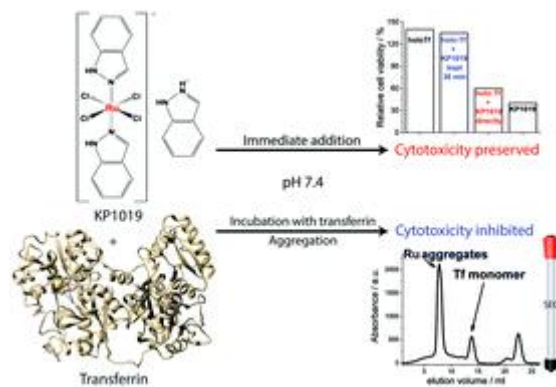
Download PDF   Article HTML

Achievement of strictly linear ultra-high molecular weight polyethylene with narrow dispersity by dint of nitro-enhanced 2,6-bis(imino)pyridylchromium chloride complexes

Chuanbing Huang, Arumugam Vignesh, Chantsalnyam Bariashir, Yanping Ma, Yang Sun and Wen-Hua Sun

The influence of reaction parameters and the electronic/steric effects of chromium complexes on the catalytic performance was investigated in detail.

From the themed collection: New Journal of Chemistry HOT Articles

The article was first published on 17 Jun 2019

Download PDF   Article HTML

Muhammad Naeem Ahmed, Khalil Ahmad, Khawaja Ansar Yasin, Tayyaba Farooq, Bilal Ahmad Khan and Soumendra K. Roy

Owing to their wide occurrence in nature and immense applications in various fields, the synthesis of aryl alkyl ethers has remained a focus of interest.
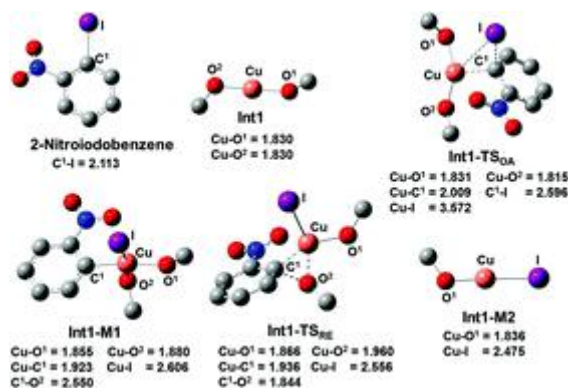
Download PDF   Article HTML

🔓 **Paper**

Investigating the effect of ligand and cation on the properties of metal fluorinated acetylacetonate based magnetic ionic liquids

Muhammad Qamar Farooq, Deepak Chand, Gabriel A. Odugbesi, Marcelino Varona, Yaroslav Mudryk and Jared L. Anderson

The effect of chemical structure on various physiochemical properties including thermal stability, solvent miscibility, magnetic susceptibility and viscosity is studied for acetylacetone based magnetic ionic liquids.
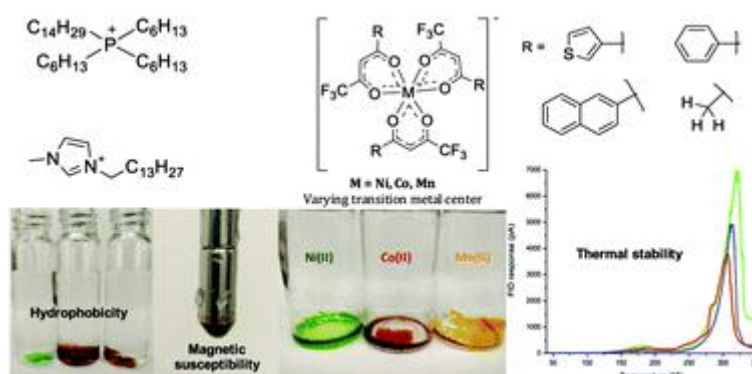
Paper

Enhanced photocatalytic activity of a pine-branch-like ternary CuO/CuS/ZnO heterostructure under visible light irradiation

Fa Cao, Zhihu Pan and Xiaohong Ji

A pine-branch-like ternary CuO/CuS/ZnO heterostructure exhibits enhanced visible light photocatalytic ability toward organic dyes.

Paper

A tetraphenylporphyrin/WO₃/exfoliated graphite nanocomposite for the photocatalytic degradation of an acid dye under visible light irradiation

Mope Edwin Malefane, Usisipho Feleni and Alex Tawanda Kuvarega

Charge carrier separation in visible light photocatalytic degradation of a dye was achieved by the fabrication of a tetraphenylporphyrin/WO₃/exfoliated graphite nanocomposite.
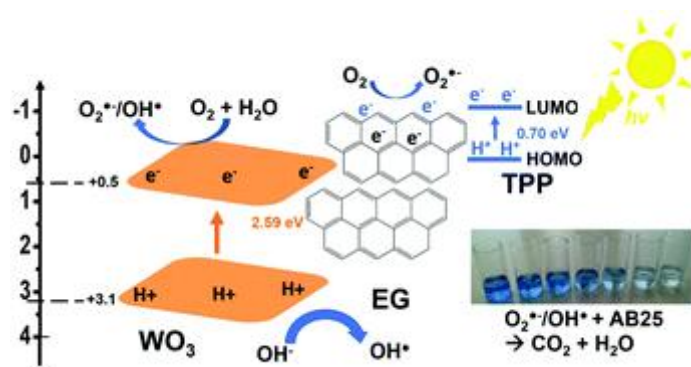
Download PDF   Article HTML

Paper

The reactivity of CO on bimetallic Ni₃M clusters (M = Sc, Ti, V, Cr, Mn, Fe, Co, Cu, Rh, Ru, Ag, Pd and Pt) by density functional theory

Ghanashyam Roy and Asoke Prasun Chattopadhyay

Surface C and O overlap with bimetallic clusters in σ, π and δ-type bonding; for example, C is a σ-donor at −15.23 eV and a π-donor at −9.29 eV, and O is a δ-acceptor at −7.76 eV in Ni₃Fe clusters.

Download PDF   Article HTML

Paper

A highly proton-/vanadium-selective perfluorosulfonic acid membrane for vanadium redox flow batteries

Xiao-Bing Yang, Lei Zhao, Kokswee Goh, Xu-Lei Sui, Ling-Hui Meng and Zhen-Bo Wang

The polar clusters of Nafion are blocked by the incorporation of the nanohybrid, which contributes to suppress vanadium ions crossover.

The article was first published on 18 Jun 2019

Download PDF   Article HTML

Perspective

2-Azaanthracenes: a chronology of synthetic approaches and bright prospects for practical applications

Olga S. Taniya, Dmitry S. Kopchuk, Albert F. Khasanov, Igor S. Kovalev, Sougata Santra, Matiur Rahman, Grigory V. Zyryanov, Adinath Majee, Valery N. Charushin and Oleg N. Chupakhin

This review aims to summarize the common synthetic approaches towards 2-azaanthracenes in chronological order, as well as systematize information on the areas of application of 2-azaanthracenes.
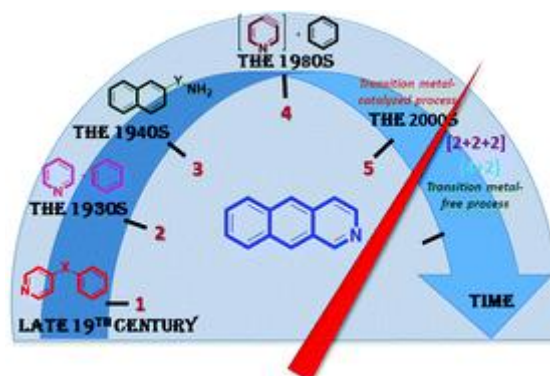
From the themed collection: 2019 Focus and Perspective articles

The article was first published on 20 Jun 2019

Download PDF   Article HTML

Paper

Synthesis, DNA and BSA binding, *in vitro* anti-proliferative and *in vivo* anti-angiogenic

In the recent times metal complexes with dual mechanisms of action, anti-cancer and anti-angiogenic, have gained substantial interest in the field of medicinal chemistry.

Complex 1: R'=CH$_3$, L= HA   Complex 2: R'=CH$_3$, L= DA   Complex 3: R'=C$_6$H$_5$, L= HA

Complex 4: R'=C$_6$H$_5$, L= DA   HA (Heptylamine):

DA(Dodecylamine):
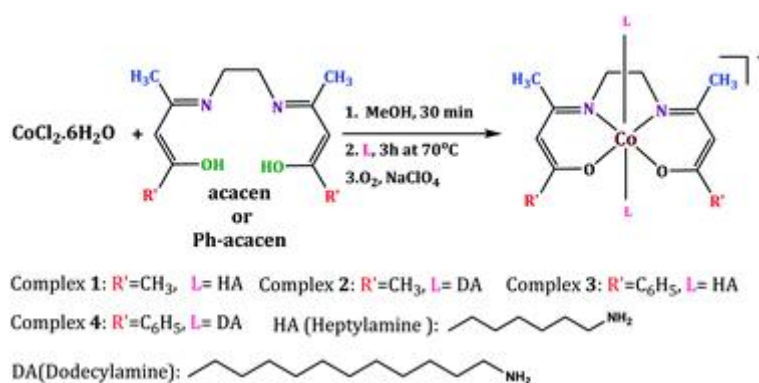
The article was first published on 20 Jun 2019

New J. Chem., 2019, **43**, 11391-11407

https://doi.org/10.1039/C9NJ01269A

Download PDF   Article HTML

Paper

Oxygen reduction reaction mechanism on a phosporus-doped pyrolyzed graphitic Fe/N/C catalyst

Hermawan K. Dipojono, Adhitya G. Saputro, Apresio K. Fajrial, Mohammad K. Agusta, Fiki T. Akbar, Febdian Rusydi and Dedy H. B. Wicaksono

The interaction between neighbouring FeN$_4$ and P$_{subs}$ sites of a P-doped pyrolyzed Fe/N/C catalyst promotes four-electron reduction through associative and dissociative mechanisms.
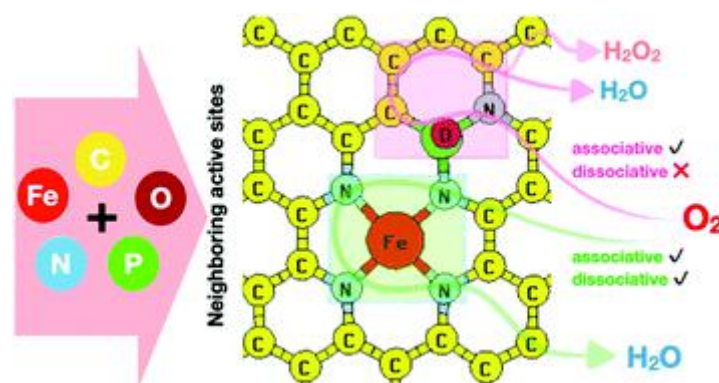
The article was first published on 25 Jun 2019

Paper

Restriction of the rotational relaxation of a butadiyne-bridged porphyrin dimer in ultrathin films

Alexander V. Shokurov, Ivan N. Meshkov, Véronique Bulach, Yulia G. Gorbunova, Mir Wais Hosseini, Aslan Yu. Tsivadze, Vladimir V. Arslanov and Sofia L. Selektor

A way to stabilize the less energetically viable orthogonal conformation of a porphyrin dimer by means of a forced orientation at an interface is shown.

Paper

Controlling the formation of self-assembled Cu–Sn sulfide with a hoya-like structure for its electrochemical performance

Xiaojuan Feng, Zhongai Hu, Yanlong Shi, Guangyue Zhao, Yi Zhou, Xiaotong Wang and Lijie Hou

Self-assembled hoya-like micron-spheres (Cu–Sn–S) with honeycomb pores were fabricated *via* a facile gelation–solvothermal–annealing three-step method and exhibited enhanced electrochemical performance for supercapacitors and HER.

Cover

Back cover

Download PDF

48 items

About New Journal of Chemistry

A journal for new directions in chemistry

Submit your article
Opens in new window

Information and templates for authors

Search this journal

Search term, DOI, author

Find an article

Year

2019

Page

e.g. 45

Go

Find issues by year (1998 - Present)

2019 - vol. 43

Journal information

About this Journal

People and Contacts

Editorial Board

Subscription Information

Follow |

Partners

Owner Societies

Spotlight

Advertisements

Top

Info

Search

NJC

Check for updates

Oxygen reduction reaction mechanism on a phosporus-doped pyrolyzed graphitic Fe/N/C catalyst†

Hermawan K. Dipojono,*[ab] Adhitya G. Saputro, [ID] *[ab] Apresio K. Fajrial, [ID] [c] Mohammad K. Agusta,[ab] Fiki T. Akbar,[d] Febdian Rusydi [ID] [ef] and Dedy H. B. Wicaksono[g]

The oxygen reduction reaction (ORR) mechanism on the active sites of a phosphorus-doped pyrolyzed Fe/N/C catalyst is examined by using density functional theory based calculations. The introduction of the phosphorus dopant creates three initial possible active sites for the ORR *i.e.*, FeN_4, C–N and P-doped sites. In the presence of O_2, the P-doped sites become passivated while the rest of the catalyst sites are still functional. The ORR profile for the associative mechanism (the O_2 molecule is reduced from its molecular form) on the FeN_4 site is practically unaffected by the presence of the neighboring P=O site. However, the ORR profile for the dissociative mechanism (the O_2 molecule is reduced from its dissociated form) on the FeN_4 site is significantly improved as compared to that on the undoped Fe/N/C catalyst system. This phenomenon is mainly induced by the distortion of C–C networks due to the presence of the neighboring FeN_4 and P=O sites, which leads to the stabilization of the *OH adsorption state on the C atoms next to the FeN_4 site.

1 Introduction

In recent years, non-precious metal catalysts (NPMCs) have drawn huge attention due to their appealing performance for the oxygen reduction reaction (ORR).[1,2] The development of NPMCs is motivated by the quest for alternative catalysts to replace scarce and costly platinum-based (Pt) materials as the cathode catalyst in hydrogen fuel cells. Pyrolyzed Fe/N/C is a type of NPMC which is fabricated by applying high temperature pyrolysis to iron/nitrogen/carbon containing moieties. Among many type of NPMCs, the pyrolzyed Fe/N/C catalyst has a promising ORR activity and high stability under fuel cell working conditions.[1,2] However, the overall performance of this catalyst has not overpowered the current state-of-the-art Pt catalyst.[3–5] Therefore, further study to improve the pyrolyzed Fe/N/C catalyst performance is very important.

Pyrolyzed Fe/N/C is a heterogeneous catalyst that consists of several types of iron–nitrogen complex (Fe–N_x) and metal-free active sites.[6–8] This fact raises several intensive discussions regarding the origin of the high catalytic activity of pyrolyzed Fe/N/C.[9–11] In addition, due to its heterogeneous nature, these active sites might be formed next to each other in the real sample. Various theoretical studies have been reported on the O_2 molecule interaction and ORR mechanism on the stand alone transition metal–nitrogen complex (TM–N_x)[12–25] or metal-free active sites.[26–39] Nonetheless, the interaction between neighboring active sites is always ignored. Our recent studies demonstrated that the interaction between neighboring active sites is actually very beneficial since it can increase their stability and the local ORR activities. We demonstrated that the interaction of the FeN_4 and quaternary-N sites at the zigzag edge of graphene could significantly improve the free energy profile for the ORR on the C atoms next to the quaternary-N site.[40] We also studied the effect of adding boron doping (B) to the pyrolyzed Fe/N/C system.[41] The formation of the neighboring FeN_4 and B–N sites not only increases the stability but also enhances the interaction between the FeN_4 site and an O_2 molecule.

[a] Research Center for Nanosciences and Nanotechnology, Institut Teknologi Bandung, Jl. Ganesha 10, Bandung 40132, Indonesia. E-mail: dipojono@tf.itb.ac.id, ganda@tf.itb.ac.id

[b] Advanced Functional Materials Research Group, Institut Teknologi Bandung, Jl. Ganesha 10, Bandung 40132, Indonesia

[c] Department of Mechanical Engineering, University of Colorado, Boulder, CO 80309, USA

[d] Theoretical High Energy Physics and Instrumentations Research Group, Institut Teknologi Bandung, Jl. Ganesha 10, Bandung 40132, Indonesia

[e] Theoretical Physics Research Group, Department of Physics, Faculty of Science and Technology, Airlangga University, Surabaya 60115, Indonesia

[f] Research Center for Quantum Engineering Design, Airlangga University, Surabaya 60115, Indonesia

[g] Department of Biomedical Engineering, Faculty of Life Sciences and Technology, Swiss German University, Tangerang 15143, Indonesia

† Electronic supplementary information (ESI) available. See DOI: 10.1039/c9nj02118c

The presence of these neighboring active sites allows the incoming O_2 molecule to be adsorbed with a side-on bridging configuration on top of the Fe and B atoms and this results in a facile O_2 dissociation process. Holby *et al.* also showed a similar trend for the O_2 interaction with the Fe–Fe atoms of neighboring FeN_x sites.[42] Obviously, these kind of interactions cannot occur in a single FeN_4 site system. All of these studies encourage, theoretically, a new strategy that might be used to improve the ORR activity of the pyrolyzed Fe/N/C-type catalyst by forming closely neighboring FeN_x and/or metal-free active sites.

Recently, catalysts made of phosphorous-doped (PG) or dual phosphorous–nitrogen-doped graphene (PNG) with various active site configurations have been reported to interact well with O_2 molecules and exhibit good ORR performance.[43–58] All of the reported active sites for PG and PNG systems maintain their graphitic structure, even though there are some distortions caused by the large atomic radii of the P atom. Inspired by the success of PG and PNG catalysts, Hu *et al.* tried to improve the ORR activity of the standard pyrolyzed Fe/N/C catalyst by introducing P doping into the catalyst.[59] They find that this catalyst has a similar onset potential to the standard pyrolyzed Fe/N/C catalyst but it has much higher current densities in the mixed kinetic and diffusion limited regions. However, the origin of this significant improvement is still unclear. The active sites of this catalyst are believed to be not significantly altered from the original active site configurations of the Fe/N/C and PNG catalysts. Therefore, the activity improvement of this catalyst might originate from the interaction of the active sites of the Fe/N/C and the PNG systems.

In this work, we study the interaction between FeN_4 and metal-free sites of the P-doped pyrolyzed Fe/N/C catalyst and its effect on their local ORR free energy profiles using density functional theory-based calculations. Since the pyrolyzed Fe/N/C catalyst has a similar graphitic structure to the P-doped graphene system, the original active site configurations can be retained in the P-doped pyrolyzed Fe/N/C system and might be formed neighboring each other. ORR mechanisms and possible thermodynamic rate-determining steps on these active sites are studied by inspecting their free energy profiles.

2 Computational details

We use one layer of a graphene 6×6 sheet with an embedded FeN_4 site as the model of the catalyst active site. It has been experimentally confirmed that the activity of the graphene system embedded with FeN_x is independent of the number of graphene layers.[60] Therefore, one layer of graphene is appropriate to model the active site structure. We choose FeN_4 to represent the FeN_x sites of the pyrolyzed Fe/N/C catalyst since this site is the most stable FeN_x configuration and active toward O_2 molecules.[23,61,62] The metal-free active site is represented by a pair of N–P atoms substituting two C atoms in the unit cell. The configuration that we used for this study is the simplest model since we only consider one N atom as the metal-free site, and one P atom as the dopant. The model of this active site

configuration is relevant to the experiment of Hu *et al.*[59] They show that the XPS profiles of P doped Fe/N/C active sites are very similar to the standard Fe/N/C and PNG catalysts. Hence, significant modifications in the structure of the active sites of the P doped Fe/N/C catalyst are not expected.

The most stable P–N pair configuration in the graphene system embedded with FeN_4 (FeN_4G-NP) is determined using two steps of substitutional atom addition.[41] The first step is done by locating one substitutional atom (either N or P) which yields the lowest total energy. From our previous study, we find that the location of the N substitutional site (N_{subs}) is almost independent of the FeN_4 site since the variation of the total energy with respect to the N_{subs}–FeN_4 distance is negligible (except when the location of the N_{subs} site is next to the N atom of the FeN_4 site the total energy of the system increases significantly).[41,63] Therefore, to obtain the most stable FeN_4G-NP configuration we only need to look at the most stable location of the P substitutional site (P_{subs}) first and then find the second substitutional site (N site) which gives the lowest total energy for the system.

Spin-polarized density functional theory[64,65] calculations are performed using the Quantum-Espresso package version 5.4.[66] Exchange and correlation effects are incorporated within the generalized gradient approximation, using the Perdew–Burke–Ernzerhof (PBE) functional.[67] Kohn–Sham eigenfuctions are expanded in plane-wave basis sets where the interactions between valence electrons and ion cores are described by ultrasoft pseudopotentials[68] taken from the Quantum-Espresso database. Converged results are achieved by using cutoff energies of 30 Ry for the plane wave and of 360 Ry for the electronic density. The effect of van der Waals interactions is described by using the semi-empirical correction scheme of Grimme, DFT-D2.[69] The Brillouin zone sampling for all systems, except isolated molecules, is performed with a $2 \times 2 \times 1$ *k*-point mesh for the structural and electronic properties. Calculations for isolated molecule are done at the gamma point in a $30 \times 30 \times 30$ Å^3 cubic cell. All of the systems are fully relaxed until the residual force on each atomic component is less than 0.025 eV Å^{-1}. The vibrational frequencies of adsorbed molecules are calculated to obtain the zero-point energy contribution in the free energy expression. In this calculation, only adsorbate vibrational modes are calculated explicitly, while the surface modes are fixed. Vibrational frequencies are computed by displacing each atom of the adsorbate by 0.01 Å in each of three cartesian directions and by diagonalizing the resulting Hessian matrix. Forces of the displaced adsorbate are calculated by the Quantum-Espresso package while the diagonalization step is performed in the Atomistic Simulation Environment (ASE).[70] Saddle points of some reactions are calculated by the climbing image nudged elastic band method (CI-NEB).[71]

The adsorption energy of a molecule on a surface is defined as:

$$E_{ad} = E_{tot} - (E_{surf} + E_{molecule}) + \Delta ZPE, \qquad (1)$$

where E_{tot} corresponds to the total energy of the combined system, E_{surf} corresponds to the total energy of the clean surface, $E_{molecule}$ corresponds to the total energy of the isolated

molecule and ΔZPE corresponds to the change in zero point energy corrections.

To calculate the change in free energy of a reaction that involves an electron transfer step, we follow the approximation in ref. 72. Briefly, the chemical potential of $[H^+ + e^-]$ under standard conditions (pH = 0, p = 1 bar, T = 298.15 K, and electrode potential U = 0 V) is related to the chemical potential of 1/2 H_2 by using the standard hydrogen electrode. The change in free energy (ΔG) of reaction $A + H^+ + e^-(U) \rightarrow AH$ is calculated using the following equation:

$$\Delta G(U) = G(AH) - G(A) - \frac{1}{2}G(H_2) - pH k_B T \ln 10 + eU, \qquad (2)$$

where $G(X)$ is the Gibbs free energy of compound X (eV) and k_B is the Boltzmann constant. This equation could be expressed as:

$$\Delta G(U) = \Delta G_0 + eU, \qquad (3)$$

where ΔG_0 is the change in free energy at electrode potential U = 0 V (short circuit condition). From this, we can see that the relation between the change in free energy and the electrode potential U within this approximation is linear. Since we are interested in the reaction in an acidic medium, we assumed that pH = 0. We also neglect the contribution from an electrochemical double layer.[72]

The overpotential of a catalyst (η) in this approximation is defined as $\eta = U^0 - U^{onset} = \Delta G_{max}(U^0)/e$.[72] U^0 represents the equilibrium potential or maximum cell voltage, which is 1.23 V. U^{onset} represents the maximum electrode potential value which makes a particular reaction pathway start to have an uphill profile (endothermic). $\Delta G_{max}(U^0)$ represents the maximum ΔG value at U = 1.23 V for a reaction in a particular reaction pathway. The thermodynamic rate-determining step (RDS) for a reaction pathway can be determined by finding a step which gives either U^{onset} or $\Delta G_{max}(U^0)$ since these quantities are linearly dependent.

3 Results and discussion

3.1 The structure of FeN$_4$G-NP

The relative energies and the location of the five most stable P$_{subs}$ sites are shown in Table 1 and Fig. 1a and b. Due to its larger atomic radius, the substitution of a C atom with a P atom distorts the local planarity of the FeN$_4$G structure (for example see Fig. 1b). Our results suggest that the stability of the system decreases as the P$_{subs}$–FeN$_4$ distance increases. In its most stable P–FeN$_4$G configuration (P1), the substitutional P atom

Table 1 Five P$_{subs}$ configurations with the lowest relative energies as indicated by the distance (Å) between P$_{subs}$ and the center of the FeN$_4$ site

P$_{subs}$ site	P$_{subs}$–FeN$_4$ (Å)	Relative energy (eV)
P1	3.168	0.00
P2	3.561	0.17
P3	2.852	0.30
P4	4.876	0.79
P5	4.876	0.85
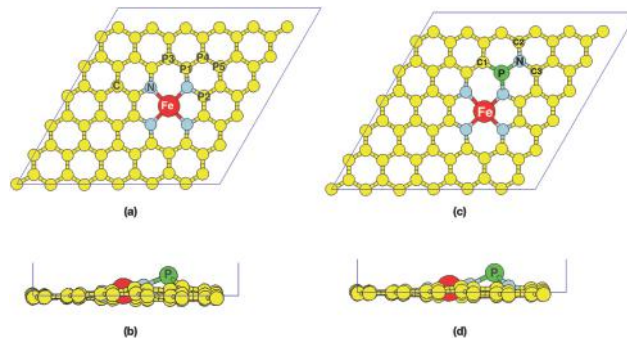
Fig. 1 (a) Location of the five most stable P$_{subs}$ sites. (b) Side view geometry of the most stable P$_{subs}$ site configuration. (c) Top-view and (d) side-view of the most stable configuration of the FeN$_4$G-NP system.

prefers to form a direct bond with the N atom of the FeN$_4$ site as shown in Fig. 1a.

The N$_{subs}$ atom is introduced into the FeN$_4$G-P system to form the FeN$_4$G-NP configuration. The location of N$_{subs}$ sites is varied and their energies are compared while keeping the position of the P1$_{subs}$ site. The most stable FeN$_4$G-NP configuration is shown in Fig. 1c and d. The structures and relative energies of less stable configurations of the other P–N pairs are shown in Fig. S1 of the ESI.† In the most stable configuration, both P$_{subs}$ and N$_{subs}$ atoms bond to each other and form a N$_{subs}$–P$_{subs}$–N link with the N atom of the FeN$_4$ site. This situation is very similar to the case of the boron (B) doped case in the FeN$_4$G-NB system[41] since B and P have similar electronegativity. The origin of this phenomenon is due to the nature of N as an electron acceptor and P as an electron donor. The P–N interaction neutralizes their presence, thereby preserving the stability of the system.

We calculate and compare the formation energies of the FeN$_4$G-NP configuration with the other active site configurations of the pyrolyzed Fe/N/C catalyst (i.e., undoped FeN$_4$G,[13,61,73,74] P-doped graphene (PG),[45,50] N-doped graphene (NG),[75–77] and PN co-doped graphene (PNG)[47]) to understand their relative stabilities. We approximate the relative formation energies of these structures based on their total energies following ref. 78 and 79 using the following equation:

$$E_{Formation} = E_{Structure} - (n_C\mu_C + n_{Fe}\mu_{Fe} + n_N\mu_N + n_P\mu_P + n_O\mu_O). \qquad (4)$$

The negative value of $E_{Formation}$ indicates that the corresponding structure might be formed spontaneously. The value of $E_{Structure}$ corresponds to the total energy of the active site structure. The values of n_C, n_{Fe}, n_N, n_P and n_O correspond to the number of C atoms, Fe atoms, N atoms, P atoms and O atoms in the unit cell.‡ μ_C, μ_{Fe}, μ_N, μ_O and μ_P correspond to the chemical potential values of the C atom, Fe atom, N atom, P atom and O atom, respectively. The values of μ_C, μ_{Fe} and μ_O are defined as the energy per C atom in pristine graphene, the energy per Fe atom in bcc bulk phase iron and the energy per O atom in an O_2 molecule, respectively. The values of μ_N and μ_P

---

‡ The presence of an O atom will be used to discuss the formation of FeN$_4$G-NP=O in the next subsection.
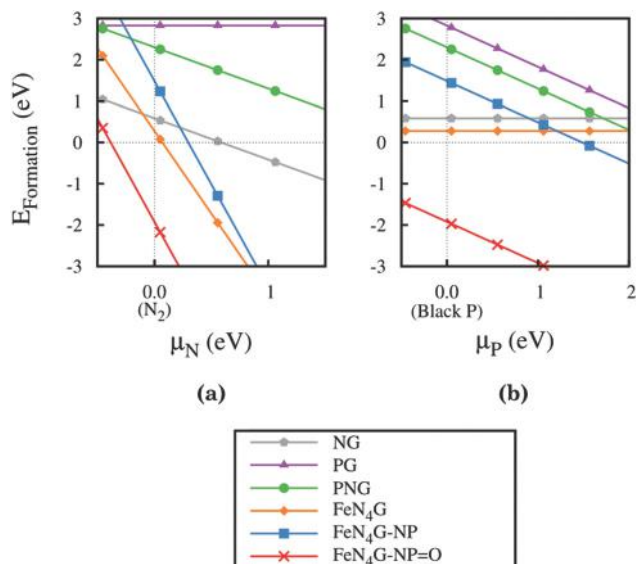
Fig. 2 Plot of the formation energy of the active site configurations as a function of (a) μ_N and (b) μ_P.

Table 2 Important results for O_2 adsorption for various active site configurations. X represents the central atoms of the active sites, which are Fe, P and C atoms for FeN_4, P_{subs} and C–N sites, respectively

Configuration	Active site	X–O (Å)	X–O–O (°)	O–O (Å)	E_{ads} O_2 (eV)	Adsorption configuration
FeN_4G-NP	FeN_4	1.836	119.53	1.316	−0.87	End-on
	P_{subs}	1.713	58.42	1.568	−1.99	Side-on
	C–N	3.166	93.23	1.251	−0.15	End-on
FeN_4G-NP=O	FeN_4	1.745	121.51	1.293	−0.95	End-on
	C–N	3.187	93.23	1.241	−0.12	End-on
FeN_4G	FeN_4	1.808	119.99	1.297	−0.96	End-on
G-N_3PO	C–N	2.900	95.42	1.259	−0.23	End-on

**Fig. 3** Top and side views of O_2 adsorption on: (a) the FeN_4 site of FeN_4G-NP, (b) the P_{subs} site of FeN_4G-NP, (c) the FeN_4 site of FeN_4G-NP=O, (d) the C–N site of FeN_4G-NP, (e) the C–N site of FeN_4G-NP=O, (f) the FeN_4 site of undoped FeN_4G and (g) the C–N site of GN_3PO.

are assumed to be tunable during experiments.[80] For reference purposes, the zero for μ_N is taken from the energy per N atom in a N_2 molecule while the zero for μ_P is taken from the energy per P atom in a bulk phase of black phosphorus.[81–83]

The results of the calculations of the formation energy as a function of μ_N and μ_P are shown in Fig. 2. According to the figure, the FeN_4G-NP configuration has an exothermic profile (negative formation energy) starting at a low μ_N value, comparable to the conventional FeN_4G active site configuration. On the other hand, the exothermic profile for this configuration arises at quite a high μ_P value, similar to the profiles of its well known metal-free versions, which are the $PG^{45,50}$ and PNG^{47} configurations. However, we should also notice from the diagram that the formation energy of the FeN_4G-NP configuration is actually much lower than that of the PG and PNG configurations, indicating that the FeN_4G-NP configuration can be formed with a higher probability. In the next subsection, we will show that the relative stability of this FeN_4G-NP configuration actually can be further improved by introducing oxygen into the system to form the FeN_4G-NP=O configuration.

3.2 O_2 adsorption on FeN_4G-NP

O_2 adsorption is one of the most important steps in the ORR process. The reduction of oxygen cannot occur without proper O_2 adsorption on the catalyst. Therefore, we begin our discussion of the ORR on the FeN_4G-NP system with the mechanism of O_2 adsorption.

Important results for the O_2 adsorption on the active site of the FeN_4G-NP system are presented in Table 2 and Fig. 3. We compare these results with the O_2 adsorption on the FeN_4 site of undoped FeN_4G and the C–N site of PN doped graphene (G-N_3PO). We specifically choose the G-N_3PO configuration to represent the active site configuration of PN doped graphene because this configuration is reported to give the lowest average ORR

overpotential over various possible P–N doping configurations.[47] The data in Table 2 show that while the O_2 adsorption energies on the FeN_4 and C–N sites of the FeN_4G-NP system are slightly weaker, its O_2 adsorption configurations are rather similar to those on the FeN_4G and G-N_3PO systems. The distortion of the C–C networks around the P_{subs} site increases the total energy of the system and this contributes to the slight weakening of the O_2–FeN_4G-NP interaction. We also find an interesting feature in the case of O_2 adsorption on the FeN_4 site of the FeN_4G-NP configuration. The O–O bond elongation in this system is larger than that on undoped FeN_4G, even though its O_2 adsorption is weaker. This condition arises due to an additional interaction between a dangling bond on the P_{subs} site and the free O atom of the adsorbed O_2 molecule. This interaction occurs through the

formation of an additional bonding state between the localized p_z orbital of the P atom and $2\pi^*$ orbitals of the adsorbed O_2 molecule (located right below the Fermi level, see Fig. S3 and S4 of the ESI†). The occupation of this state enhances the repulsion between the O atoms of the adsorbed O_2 molecule and results in the extra elongation of the O–O bond. This kind of mechanism is absent for the case of O_2 adsorption on the undoped FeN$_4$G configuration.

We also investigate the adsorption of an O_2 molecule on top of the P$_{subs}$ site. We find that the O_2 molecule is adsorbed on this site with side-on adsorption and a very large O–O bond elongation (see Fig. 3b), similar to the case of O_2 adsorption on P doped graphene.[50] Evidently, from Table 2 we can see that this configuration is the most stable O_2 adsorption configuration on the FeN$_4$G-NP system, with an adsorption strength twice of that on the FeN$_4$ site. This finding suggests that the incoming O_2 molecule will likely approach the P$_{subs}$ site with higher probability than the other two adsorption sites. The formation of O_2 side-on adsorption on the P$_{subs}$ site arises from the interactions of the localized p_z state of the P atom and the bonding orbitals of the O_2 molecule (2π and 2σ). The bonding states resulting from these interactions are shown in Fig. S5 of the ESI.†

We perform an O_2 dissociation calculation on the P$_{subs}$ site to check the stability of the adsorbed O_2 since its O–O bond is highly elongated. In the final state, we find that one of the O atoms of the adsorbed O_2 molecule stays at the P$_{subs}$ site and the other one prefers to move to the top of the Fe atom of the FeN$_4$ site (2O–FeN$_4$-NP configuration). Our calculation shows that this dissociation reaction is actually a barrierless process. This result suggests that an incoming O_2 molecule approaching the P$_{subs}$ site of the FeN$_4$-NP system will not stay adsorbed on the P atom in its molecular form, instead it will spontaneously dissociate and directly form a 2O–FeN$_4$-NP configuration.

We also calculate the energies required for removing one O atom from the 2O–FeN$_4$-NP configuration to estimate the stability of the adsorbed O atom on the FeN$_4$ site and P$_{subs}$ site. The energies required for removing one O atom from the FeN$_4$ site and P site in the 2O–FeN$_4$-NP configuration are found to be −1.13 eV and −3.30 eV, respectively. As we will discuss in the next subsection, the adsorbed O atom on the FeN$_4$ site can be reduced easily into water due to its weaker adsorption strength. However, this is not the case for the adsorbed O atom on the P$_{subs}$ site. The formation of the P=O configuration stabilizes the localized p_z state of the P$_{subs}$ site (through the $p_z^P + p_z^O$ interaction) away from the Fermi level as indicated in Fig. S6 of the ESI.† This interaction makes the P=O bond become very strong and difficult to dissociate ($E_{ad}^O \sim$ −3.30 eV). Moreover, our calculation shows that the reduction of *O on the P$_{subs}$ site into *OH has a very endothermic profile even at $U = 0$ V ($\Delta G = 0.95$ eV), indicating a difficult reduction process. Hence, the first reduction step will prefer the complete reduction of *O on the FeN$_4$ site into water over the reduction of *O on the P$_{subs}$ site. This reaction will leave us only with a very stable O atom adsorbed on the P$_{subs}$ site of the FeN$_4$-NP configuration. If the subsequent reaction ought to proceed, it will be a competition between two possible reactions: (1) reduction of the P=O

configuration into P–OH or (2) O_2 adsorption on the empty FeN$_4$ site. The system will most likely prefer the O_2 adsorption since this is not an activated process, as compared to the reduction of the P–O configuration. Therefore, the P=O configuration can be considered as a stable configuration acknowledging the strong adsorption of the O atom on the P$_{subs}$ site. This configuration is referred to as the FeN$_4$G-NP=O configuration. A simplified schematic of the formation of this FeN$_4$G-NP=O configuration is shown in Fig. 4.

We calculate the formation energy for the FeN$_4$G-NP=O configuration to see the effect of the adsorbed O atom on the P$_{subs}$ site. We observe that the termination of the dangling bond on the P$_{subs}$ site by forming a P=O bond stabilizes the system. This result is shown in Fig. 2. We can see that the FeN$_4$G-NP=O configuration already has an exothermic profile even at very low μ_N and μ_P values. This finding also suggests that the FeN$_4$G-NP=O configuration can be formed easily with a higher probability as compared to the other active site configurations if an O_2 molecule is involved in the formation process. The formation of the graphitic P–O structure is in line with the appearance of P–C and P–O peaks in the P 2p XPS spectra of the P doped Fe/N/C catalyst.[59,84] Therefore, from this point we will use the FeN$_4$G-NP=O configuration as the main active site structure for the ORR process.

We calculate the O_2 adsorption on the possible active sites of the FeN$_4$G-NP=O configuration. Initially, there are three possible active sites for O_2 adsorption on the original FeN$_4$G-NP configuration as listed in Table 2. However, in the FeN$_4$G-NP=O configuration the P$_{subs}$ site is not available for O_2 adsorption since it is passivated by an O atom. Therefore, only two possible sites are available for O_2 adsorption for this configuration: (1) the FeN$_4$ site and (2) the C atoms around the NP=O site. Results of O_2 adsorption on these sites are given in Table 2.

As in the case of the FeN$_4$G-NP configuration, we find that an O_2 molecule is strongly adsorbed on the FeN$_4$ site of the
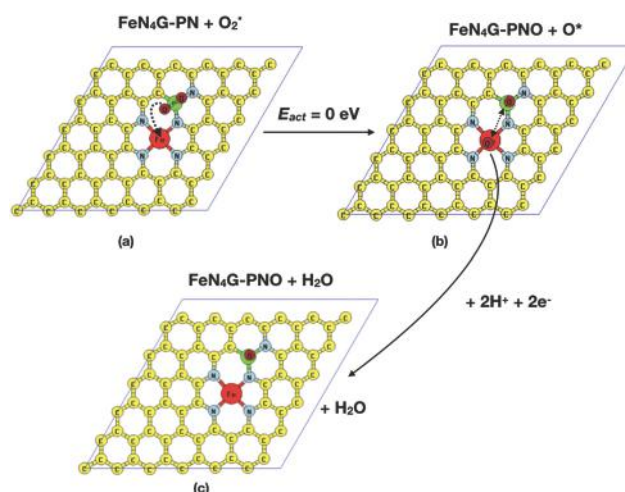

Fig. 4 A simplified schematic of the formation of the FeN$_4$G-NP=O configuration. (a) O_2 side-on adsorption on the P$_{subs}$ site, (b) the dissociation of the adsorbed O_2 molecule and (c) the reduction of the adsorbed O atom on the FeN$_4$ site.

FeN$_4$G-NP=O configuration while it is only weakly physisorbed on the C–N site. However, the O–O bond elongation on the FeN$_4$ site of the FeN$_4$G-NP=O configuration is quite similar to that on the FeN$_4$ site of the undoped FeN$_4$G configuration. This is because, in contrast with the case of O$_2$ adsorption on the FeN$_4$G-NP configuration, the localized p$_z$ state of the P$_{subs}$ site of the FeN$_4$G-NP=O configuration cannot interfere with the adsorbed O$_2$ molecule on the FeN$_4$ site since it is already stabilized by the adsorbed O atom. In addition to this, due to steric hindrance, the free O atom of the adsorbed O$_2$ has to face the opposite direction to the P–O site. This adsorption configuration is shown in Fig. 3c. The O$_2$ adsorption energy and the end-on adsorption configuration on the FeN$_4$ site of FeN$_4$G-NP=O are very similar to the O$_2$ adsorption on typical FeN$_4$ active site configurations such as in FeN$_4$G,[13,14,22,23] Fe porphyrin[85,86] and Fe tape-porphyrin[87] systems.
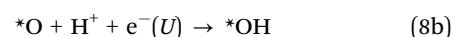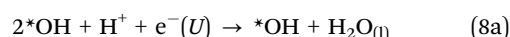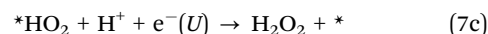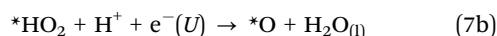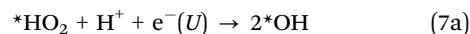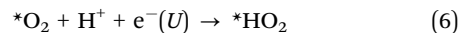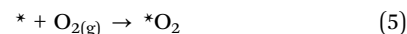
For the case of adsorption on the C–N site, even though the O$_2$ molecule is only weakly physisorbed, the O$_2$ adsorption energy on the C–N site of the FeN$_4$G-NP=O configuration is slightly weaker than that of the G-N$_3$PO configuration. A theoretical study conducted by Gracia-Espino shows that P–N doped graphene works best towards the ORR only when the N$_{subs}$ sites are not in direct contact with the P=O site, since this will bring the localized states of the C atoms around the N$_{subs}$ and P=O toward the Fermi level, which will facilitate the C–O$_2$ interaction.[47] However, when the N$_{subs}$ site is close to the P=O site, the localized states of the surrounding C atoms will be shifted far from the Fermi level and this will hinder the C–O$_2$ interaction. This mechanism explains why the O$_2$ molecule adsorption energy on the C–N site of the FeN$_4$G-NP=O configuration is weaker than that of the G-N$_3$PO configuration since the N$_{subs}$ site of the FeN$_4$G-NP=O configuration is directly bonded to its P=O site. A comparison of the O$_2$ adsorption configuration on the C–N site of the FeN$_4$G-NP=O and G-N$_3$PO configurations is shown in Fig. 3e and g.

3.3 ORR mechanism on FeN$_4$G-NP=O

In this section we will only discuss the ORR mechanism on the FeN$_4$G-NP=O configuration since the P$_{subs}$ site of the FeN$_4$G-NP configuration will always be poisoned by an O atom when an O$_2$ molecule interacts with this site. In the previous subsection, we find two stable O$_2$ adsorption configurations that exist on the FeN$_4$G-NP=O system: (1) strong end-on adsorption on the FeN$_4$ site and (2) weak physisorption on the C–N site. In general, there are two possible mechanisms for the ORR: associative and dissociative mechanisms. The main difference lies in the involvement of direct dissociation of the adsorbed O$_2$ molecule for the dissociative mechanism. The associative mechanism could happen on the FeN$_4$ and C–N sites. However, the dissociative mechanism could only happen on the FeN$_4$ site since no noticeable O–O elongation exists in the O$_2$ physisorption on the C–N site. We will also compare the ORR profiles for the related reduction mechanism on the FeN$_4$ site of the undoped FeN$_4$G system and the C–N site of the G-N$_3$PO system.

3.3.1 Associative mechanism. We calculate the ORR free energy profiles for the following reactions, which represent the

associative mechanisms on the FeN$_4$ site of the FeN$_4$G and FeN$_4$G-NP=O systems and the C–N site of the G-N$_3$PO and FeN$_4$G-NP=O systems:

$$* + O_{2(g)} \rightarrow *O_2 \qquad (5)$$

$$*O_2 + H^+ + e^-(U) \rightarrow *HO_2 \qquad (6)$$

$$*HO_2 + H^+ + e^-(U) \rightarrow 2*OH \qquad (7a)$$

$$*HO_2 + H^+ + e^-(U) \rightarrow *O + H_2O_{(l)} \qquad (7b)$$

$$*HO_2 + H^+ + e^-(U) \rightarrow H_2O_2 + * \qquad (7c)$$

$$2*OH + H^+ + e^-(U) \rightarrow *OH + H_2O_{(l)} \qquad (8a)$$

$$*O + H^+ + e^-(U) \rightarrow *OH \qquad (8b)$$

$$*OH + H^+ + e^-(U) \rightarrow H_2O_{(l)} + *, \qquad (9)$$

where * represents an empty adsorption site and *X represents an adsorbed X species.

The direct four-electron reduction pathway to form water is composed of two main branches:

A (5) → (6) → (7a) → (8a) → (9)

B (5) → (6) → (7b) → (8b) → (9).
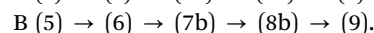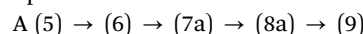
Reaction pathways A and B mainly differ in the formation of 2*OH (7b) and *O + H$_2$O (7a), respectively. We also calculate the ORR profiles for the possible two-electron reduction pathway to produce H$_2$O$_2$, which is represented by the following sequence:

C (5) → (6) → (7c).
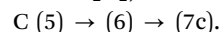
The calculated ORR profiles for the associative mechanism on the FeN$_4$ and C–N sites at U = 0 V are shown in Fig. 5 and 6, respectively. The ORR profiles at equilibrium potential U = 1.23 V are presented in Section S4 of the ESI.†

For the case of the FeN$_4$ site, all of the reaction steps are found to have downhill profiles on both reaction pathways. We find that a H$_2$O$_2$ molecule cannot be formed on the FeN$_4$ site of the FeN$_4$G-NP=O system from the *HO$_2$ + H$^+$ + e$^-$ reaction since the adsorbed molecule will dissociate spontaneously into 2*OH or *O + H$_2$O. This situation is similar to the undoped

Fig. 5 ORR energy profiles for the associative mechanism on the FeN$_4$ site of the FeN$_4$G-NP=O system compared to that of the undoped FeN$_4$G system.

Fig. 6 ORR energy profiles for the associative mechanism on the C–N site of the FeN_4G-NP=O system compared to that of the G-N_3PO system.
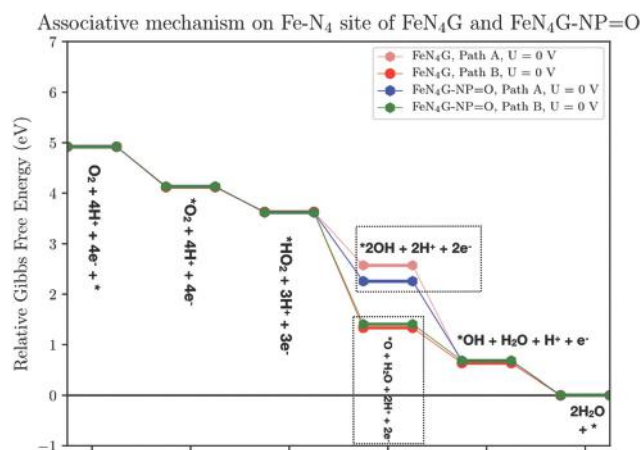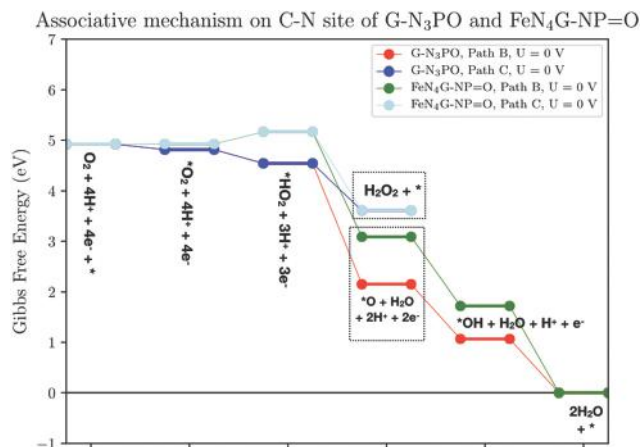
FeN_4G system.[22,40] This result supports the experimental finding that shows a very low H_2O_2 yield on the P doped Fe/N/C catalyst.[59] On this catalyst, the H_2O_2 molecule can only be formed on the C–N and C–N–P=O active sites as we will demonstrate in the following paragraphs. From Fig. 5, we can see that the FeN_4G-NP=O system has a similar ORR profile to the undoped FeN_4G system since the energy plots almost coincide for all reaction steps, except for the 2*OH adsorption state. The 2*OH adsorption state on the FeN_4 site of the FeN_4G-NP=O system is more stable because the H atom from one of the formed *OH weakly interacts with the O atom of the P=O site (see Fig. S10 of the ESI†). This interaction makes the *OH adsorption state become more stable. Such an interaction is absent in the case of 2*OH adsorption on the undoped FeN_4G system.

The calculated onset potential (U^{onset}) and overpotential (η) for the associative mechanism through both reaction pathways on the FeN_4 site of the FeN_4G and FeN_4G-NP=O systems are tabulated in Table 3. U^{onset} for the FeN_4G and FeN_4G-NP=O systems is 0.49 V and 0.51 V, corresponding to η values of 0.74 V and 0.72 V, respectively. The thermodynamic RDS for the ORR on these systems can be determined by locating the reactions

which give U^{onset}. The RDS for both systems is caused by reaction (6), which is *O_2 reduction to *HO_2. The FeN_4G-NP=O system has a better η value (~ 0.02 V) because the *HO_2 adsorption state on this system is more stable.

From the above discussions, the presence of the P=O site does not negatively affect the ORR profile of the FeN_4 site for the associative mechanism. Instead, we find some slight improvement in the ORR profiles of the FeN_4G-NP=O and undoped FeN_4G configurations. In general, the overpotential and RDS for the FeN_4 site of the FeN_4G-NP=O system still remain comparable with the FeN_4 site of the typical FeN_4G system.[23,40,88]

For the case of the associative mechanism on the C–N site of the FeN_4G-NP=O system, we find that only the first hydrogenation step to form HO_2 (reaction (6)) has an uphill profile while the rest of the reactions have downhill profiles at $U = 0$ V. This is very different from the G-N_3PO system where all the reaction steps have downhill profiles. This behavior is expected since the C–N site of the FeN_4G-NP=O system cannot properly adsorb an O_2 molecule as discussed before, in contrast with the C–N site of the G-N_3PO system. This weak interaction hinders the reduction step of O_2 into HO_2. We also find that the H_2O_2 formation (pathway C) has a downhill profile on the C–N site. However, the H_2O_2 dissociation into 2*OH cannot occur on the C–N site due to the weak surface–adsorbate interaction. Therefore, this indicates that even though the ORR profile on this C–N site is energetically unfavorable, the two-electron reduction mechanism to form a H_2O_2 molecule could happen on this site, in addition to the direct $4e^-$ reduction mechanism to form water through the reduction of *HO_2 into *O + H_2O (pathway B), if the O_2 molecule somehow can bind to the site. As we mentioned previously, these C–N and C–N–P=O sites are responsible for formation of a very small H_2O_2 yield observed in the experiment.[59] Unfortunately, the formation of this ORR side product, H_2O_2, is not very beneficial for the fuel cell system since it will slow down the total ORR kinetics and the produced H_2O_2 will cause the degradation of perfluorinated sulfonic acid (PFSA) membranes.[89–91]

The calculated U^{onset} for the ORR on the C–N site of the G-N_3PO and FeN_4G-NP=O systems is 0.27 V and -0.24 V, corresponding to η values of 0.96 V and 1.47 V, respectively. The thermodynamic RDS for the ORR on these systems is also caused by reaction (6), the *O_2 reduction to *HO_2. The C–N site of the FeN_4G-NP=O system has a very high η because of the uphill profile that exists at $U = 0$ V. The high η value of the FeN_4G-NP=O system indicates that the C–N site of the system has worse ORR performance than that of the G-N_3PO system. The calculated U^{onset} for the ORR on the C–N site of the G-N_3PO and FeN_4G-NP=O systems is comparable with that on the P–C site of the P doped graphene (PG) system (0.1–0.27 V).[49] However, the RDS for the PG system originates from the hydrogenation of *OH into H_2O.

3.3.2 Dissociative mechanism. In this section we discuss the dissociative mechanism on the FeN_4 site of the FeN_4G and FeN_4G-NP=O systems. The dissociative mechanism on the C–N site is not considered due to its weak interaction with O_2 molecules.

Table 3 Onset potential (U^{onset}), overpotential (η) and rate determining-step (RDS) for the ORR on selected active sites

System	Active site	ORR mechanism	Reaction pathway	U^{onset}(V)	η(V)	RDS
FeN_4G-PN=O	FeN_4	Associative	A	0.51	0.72	(6)
			B	0.51	0.72	(6)
		Dissociative	D	0.83	0.40	(14a)
			E	0.68	0.55	(15b)
	C–N	Associative	B	−0.24	1.47	(6)
			C	−0.24	1.47	(6)
FeN_4G	FeN_4	Associative	A	0.49	0.74	(6)
			B	0.49	0.74	(6)
		Dissociative	D	0.30	0.93	(14a)
			E	0.63	0.60	(15b)
G-N_3PO	C–N	Associative	B	0.27	0.96	(6)
			C	0.27	0.96	(6)

A very high activation energy is expected for the O_2 dissociation on this C–N site.

For the case of the FeN_4 site, the O_2 dissociation begins from the O_2 end-on adsorption state. The surface unbound O atom of the adsorbed O_2 molecule attacks the nearest C–C bond during the dissociation process. This dissociation results in an Fe–O bond at the FeN_4 site and C–O bonds at the C–C networks as shown in Fig. S11 of the ESI.† The activation energies for O_2 dissociation on the FeN_4 site of the FeN_4G and FeN_4G-NP=O systems are about 1.05 eV and 1.01 eV, respectively. These values are comparable with a previous DFT calculation by Orellana for O_2 dissociation on the FeN_4G system (1.10 eV).[13]

Starting from the 2*O configuration, there are two possibilities for the subsequent reduction reactions. The reaction either starts from the reduction of *O on the Fe site or from *O on the C site. The dissociative mechanisms on the FeN_4 site of the FeN_4G and FeN_4G-NP=O systems are composed of the following reactions:

$$* + O_{2(g)} \rightarrow *O_2 \qquad (10)$$

$$*O_2 \rightarrow *O^{[Fe]} + *O^{[C]} \qquad (11)$$

$$*O^{[Fe]} + *O^{[C]} + H^+ + e^-(U) \rightarrow *OH^{[Fe]} + *O^{[C]} \qquad (12a)$$

$$*O^{[Fe]} + *O^{[C]} + H^+ + e^-(U) \rightarrow *O^{[Fe]} + *OH^{[C]} \qquad (12b)$$

$$*OH^{[Fe]} + *O^{[C]} + H^+ + e^-(U) \rightarrow *O^{[C]} + H_2O_{(l)} \qquad (13a)$$

$$*O^{[Fe]} + *OH^{[C]} + H^+ + e^-(U) \rightarrow *O^{[Fe]} + H_2O_{(l)} \qquad (13b)$$

$$*O^{[C]} + H^+ + e^-(U) \rightarrow *OH^{[C]} \qquad (14a)$$

$$*O^{[Fe]} + H^+ + e^-(U) \rightarrow *OH^{[Fe]} \qquad (14b)$$

$$*OH^{[C]} + H^+ + e^-(U) \rightarrow H_2O_{(l)} + *, \qquad (15a)$$

$$*OH^{[Fe]} + H^+ + e^-(U) \rightarrow H_2O_{(l)} + *, \qquad (15b)$$
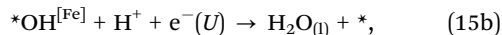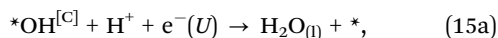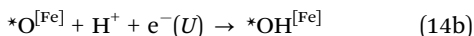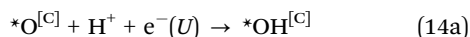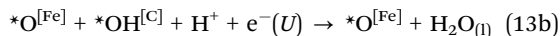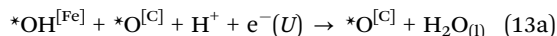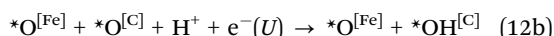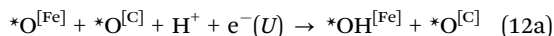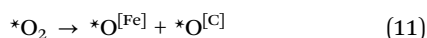
where $*X^{[Y]}$ represents an adsorbed X species on the Y site.

These reactions consist of two main branches:

D (10) → (11) → (12a) → (13a) → (14a) → (15a)
E (10) → (11) → (12b) → (13b) → (14b) → (15b)
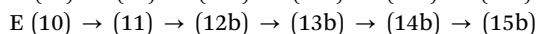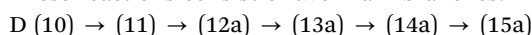
These reaction pathways only differ in the order of the reduction sites. The calculated ORR profiles for the dissociative mechanisms on the FeN_4 site at $U = 0$ V through paths D and E are shown in Fig. 7. The ORR profiles at equilibrium potential $U = 1.23$ V are presented in Section S4 of the ESI.†

We find that all of the reduction steps have downhill profiles at $U = 0$ V. The ORR profiles for both of the FeN_4G and FeN_4G-NP=O systems are also quite similar, except for the second *O reduction step on the C site (reaction (14a)). Reaction (14a) on the FeN_4G-NP=O system is more exothermic than that on the FeN_4G system. This is because the *OH adsorption state on the C–C networks of the FeN_4G-NP=O system is much more stable than that of the FeN_4G system. In contrast to the undoped FeN_4G system, the co-existence of the neighboring FeN_4 and P=O sites in the FeN_4G-NP=O system perturbs the local planarity of the surrounding C–C networks. The distortion of the C–C networks facilitates the C atoms to interact with the adsorbate and this interaction will result in a relatively more
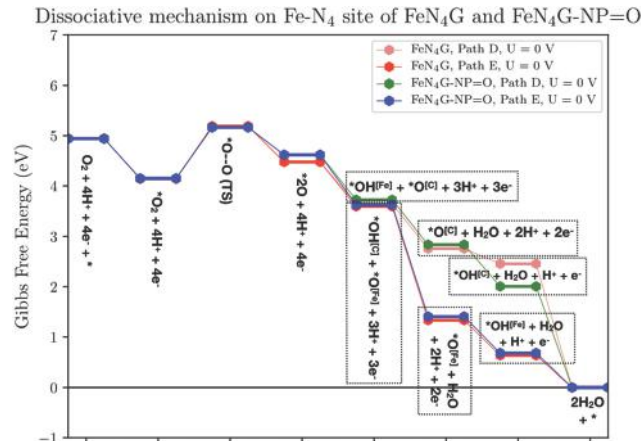
Fig. 7 ORR energy profiles for the dissociative mechanism on the FeN_4 site of the FeN_4G-NP=O system compared to that of the undoped FeN_4G system.

stable adsorption state as compared to the adsorption on the undoped FeN_4G system. The adsorption configuration of OH on this C site is shown in Fig. S12 of the ESI.† A similar mechanism also occurs in the interaction between the neighboring quaternary-N (C–N–C) and FeN_4 sites at the zigzag edge of graphene.[40] The distortion caused by this interaction also stabilizes the *OH adsorption state on the C atom of the C–N–C site.

The calculated U^{onset} and η for the dissociative mechanism through the two reaction pathways on the FeN_4G and FeN_4G-NP=O systems are tabulated in Table 3. We find that these pathways have different η and thermodynamic RDSs, unlike the case of the associative mechanism where all pathways share the same RDS. This is because the inclusion of O_2 dissociation bypasses the HO_2 formation step, which is the common RDS for the associative mechanism on the FeN_4 site. The RDSs for the dissociative mechanisms are shifted to reactions (14a) and (15b) for pathways D and E, respectively.

We find that the difference in η for pathway E on the FeN_4G-NP=O and FeN_4G systems is modest, on the order of ~ 0.05 V. This is because the RDS of this pathway is the reduction of *OH into water on the FeN_4 site, which has similar ΔG values for both systems. This reduction step is identical to reaction (9) of the associative mechanism (see Fig. 5). The more profound difference is found in pathway D. η for pathway D on the FeN_4G-NP=O system is much lower than that on the FeN_4G system. The RDS for this pathway is the reduction of *O into *OH on the C site. The value of ΔG for this step is again related to the *OH adsorption strength on the C site of the system. The stabilization of the *OH adsorption state on the FeN_4G-NP=O system makes this system have a much better η value.

3.4 Discussion

The results from this study can be used to explain the ORR activity trend found in the experiment by Hu *et al.*[59] First, they find that the P doped pyrolyzed Fe/N/C catalyst has a similar onset potential to the standard pyrolyzed Fe/N/C catalyst. Our

calculation result on the associative mechanism on the FeN$_4$ site of the FeN$_4$G-NP=O system is in agreement with their finding. We find that the presence of the P=O site does not disturb the electronic structure of the FeN$_4$ site. It causes the ORR profile for the associative mechanism on the FeN$_4$ site of the FeN$_4$G-NP=O system to become similar to that of the undoped FeN$_4$G system and hence results in a quite similar onset potential. Since the FeN$_4$G configuration is known as the active site of the typical pyrolyzed Fe/N/C catalyst, this finding explains why the P doped Fe/N/C catalyst has a similar onset potential to the undoped one. Second, they find that the P doped pyrolyzed Fe/N/C catalyst has much higher current densities than the standard pyrolyzed Fe/N/C catalyst. This improvement is attributed to the increase in the active site density of the catalyst through the formation of various metal free sites such as C–N, C–P, and C–P–N active sites in addition to the FeN$_x$ active sites.[59] Our calculations show that these metal free sites could catalyze the ORR quite well, although some of them prefer to produce peroxide instead of water. Another contributing factor is the activation of the ORR dissociation pathway on the FeN$_4$ site of the FeN$_4$G-NP=O system. Although this pathway is slightly hindered by the O$_2$ dissociation step, the positive interaction between the FeN$_4$ and the P=O sites improves the ORR profile for the pathway quite significantly as compared to the undoped FeN$_4$G system. This interaction makes both the associative and dissociative pathways become viable, hence improving the flexibility of the FeN$_4$ site towards the ORR. These mentioned factors allow the catalyst to produce a better current profile than the standard pyrolyzed Fe/N/C catalyst.

From our computational results, we can also extract important insights that can be used as a new strategy to improve the ORR profile of the neighboring TM–N$_4$ and metal-free active sites of the pyrolyzed TM/N/C-based catalyst. These insights can be obtained from the ORR profile of the FeN$_4$G-NP=O system through the dissociation mechanism. We find a significant improvement in the η value since the RDS for this pathway involves the reduction of *O into *OH on the C atom next to the FeN$_4$ site. Unlike the case of the FeN$_4$ site, the ΔG profile for this step on the C site of the FeN$_4$G-NP=O system differs significantly from that of the undoped FeN$_4$G system. The value of ΔG for this step on the FeN$_4$G-NP=O system is more exothermic due to the significant stabilization of the *OH adsorption state on the C atom, which is induced by distortion of the local planarity of the C–C networks around the neighboring FeN$_4$ and P=O sites as discussed before. This finding suggests that the ORR profiles of the O$_2$ dissociative mechanism, which involves a TM–N$_4$ and a C–C site, might be improved if the local planarity of the C–C networks is distorted. Various type of defects such as point defects or substitutional defects are able to distort the planarity of a graphene system.[50,55,92–98] Such defects might also be introduced near the TM–N$_4$ site to distort the local planarity of the C–C networks of the TM–N$_4$G system since this system also exhibits a graphitic structure. In addition to this mechanism, we also need to consider the activation energy for O$_2$ dissociation on the TM–N$_4$ site. Even though the dissociation mechanism gives a low η for the FeN$_4$G-NP=O system, it is slightly difficult for this mechanism to occur since it requires a moderate O$_2$ dissociation energy to initiate the reaction. The ORR through the dissociation mechanism will be more feasible if we can reduce the activation energy for O$_2$ dissociation. This requirement might be achieved by changing the transition metal type,[13,14,19,86] or by using other TM–N$_x$ configurations.[18,42,73] Therefore, the ORR profile *via* the dissociation mechanism might be improved by combining the following conditions: (1) lowering the O$_2$ dissociation energy through the modification of the TM–N$_x$ structure and (2) stabilizing the *OH adsorption state by distorting the local planarity of the C–C networks around the TM–N$_x$ site.

4 Summary

The ORR mechanism on the active sites of a P-doped pyrolyzed Fe/N/C catalyst has been studied by using density functional theory based calculations. The FeN$_4$ site forms a direct bond with the P$_{subs}$ and N$_{subs}$ sites in the most stable active site configuration. Initially there are three possible active sites for this system, which are the FeN$_4$, C–N and P$_{subs}$ sites. Interaction of the P$_{subs}$ site with an O$_2$ molecule modifies the site into an inherently stable P=O configuration, which is less active toward O$_2$ molecules. Moreover, due to the formation of direct bonding between N$_{subs}$ and P$_{subs}$ sites, the surrounding C–N sites become discouraged to interact properly with the incoming O$_2$ molecule. Even so, the FeN$_4$ site is still able to effectively reduce O$_2$ molecules into water on this system.

We find that the presence of neighboring metal-free active sites does not significantly alter the electronic structure of the FeN$_4$ site of the FeN$_4$G-NP=O system. Due to this observation, the properties of atomic or molecular adsorption on the FeN$_4$ site of this system become similar to that on the undoped FeN$_4$G system. The same situation also occurs in the ORR profiles for the associative mechanism since all of the involved reactions proceed on top of the Fe atom of the FeN$_4$ configuration. In contrast, the dissociative mechanism produces different ORR profiles since this reduction mechanism involves both the FeN$_4$ site and the neighboring C–C networks. The presence of the neighboring FeN$_4$ and P=O sites in the FeN$_4$G-NP=O system distorts the local planarity of the C–C networks around them and this distortion stabilizes the *OH adsorption state on the C site. Such stabilization contributes to a significant improvement in the ORR profiles for the dissociative mechanism, even though this mechanism still requires a high activation energy for the O$_2$ dissociation step.

Using the insights obtained from our results, we also proposed a new strategy to make the ORR dissociation mechanism become more feasible on the active sites of pyrolyzed TM/N/C catalysts. The ORR profile *via* the dissociation mechanism might be improved by combining the following conditions: (1) lowering the O$_2$ dissociation energy through the modification of the TM–N$_x$ structure and (2) stabilizing the *OH adsorption state on the C site by distorting the local planarity of the C–C networks around the TM–N$_x$ site through substitutional doping or point defects.

Conflicts of interest

There are no conflicts to declare.

Acknowledgements

Notes and references

1 M. Shao, Q. Chang, J.-P. Dodelet and R. Chenitz, *Chem. Rev.*, 2016, **116**, 3594–3657.

2 A. A. Gewirth, J. A. Varnell and A. M. DiAscro, *Chem. Rev.*, 2018, **118**, 2313–2339.

3 F. Jaouen, E. Proietti, M. Lefevre, R. Chenitz, J.-P. Dodelet, G. Wu, H. T. Chung, C. M. Johnston and P. Zelenay, *Energy Environ. Sci.*, 2011, **4**, 114–130.

4 G. Wu, K. L. More, C. M. Johnston and P. Zelenay, *Science*, 2011, **332**, 443–447.

5 M. Lefèvre, E. Proietti, F. Jaouen and J.-P. Dodelet, *Science*, 2009, **324**, 71–74.

6 Z. Chen, D. Higgins, A. Yu, L. Zhang and J. Zhang, *Energy Environ. Sci.*, 2011, **4**, 3167–3192.

7 C. Medard, M. Lefévre, J. Dodelet, F. Jaouen and G. Lindbergh, *Electrochim. Acta*, 2006, **51**, 3202–3213.

8 J. M. Ziegelbauer, T. S. Olson, S. Pylypenko, F. Alamgir, C. Jaye, P. Atanassov and S. Mukerjee, *J. Phys. Chem. C*, 2008, **112**, 8839–8849.

9 Q. Jia, N. Ramaswamy, U. Tylus, K. Strickland, J. Li, A. Serov, K. Artyushkova, P. Atanassov, J. Anibal, C. Gumeci, S. C. Barton, M.-T. Sougrati, F. Jaouen, B. Halevi and S. Mukerjee, *Nano Energy*, 2016, **29**, 65–82.

10 D. Guo, R. Shibuya, C. Akiba, S. Saji, T. Kondo and J. Nakamura, *Science*, 2016, **351**, 361–365.

11 W. Liu, L. Zhang, X. Liu, X. Liu, X. Yang, S. Miao, W. Wang, A. Wang and T. Zhang, *J. Am. Chem. Soc.*, 2017, **139**, 10790–10798.

12 D. H. Lee, W. J. Lee, W. J. Lee, S. O. Kim and Y.-H. Kim, *Phys. Rev. Lett.*, 2011, **106**, 175502.

13 W. Orellana, *J. Phys. Chem. C*, 2013, **117**, 9812–9818.

14 F. Calle-Vallejo, J. I. Martinez and J. Rossmeisl, *Phys. Chem. Chem. Phys.*, 2011, **13**, 15639–15643.

15 H. K. Dipojono, A. G. Saputro, R. Belkada, H. Nakanishi, H. Kasai, M. David and E. Sy Dy, *J. Phys. Soc. Jpn.*, 2009, **78**, 094710.

16 H. K. Dipojono, A. G. Saputro, S. M. Aspera and H. Kasai, *Jpn. J. Appl. Phys.*, 2011, **50**, 055702.

17 A. G. Saputro, F. Rusydi, H. Kasai and H. K. Dipojono, *J. Phys. Soc. Jpn.*, 2012, **81**, 034703.

18 A. G. Saputro and H. Kasai, *J. Phys. Soc. Jpn.*, 2014, **83**, 024707.

19 A. G. Saputro, H. Kasai, K. Asazawa, H. Kishi and H. Tanaka, *J. Phys. Soc. Jpn.*, 2013, **82**, 114704.

20 S. Kattel, P. Atanassov and B. Kiefer, *Phys. Chem. Chem. Phys.*, 2013, **15**, 148–153.

21 S. Kattel, P. Atanassov and B. Kiefer, *J. Phys. Chem. C*, 2012, **116**, 17378–17383.

22 S. Kattel and G. Wang, *J. Phys. Chem. Lett.*, 2014, **5**, 452–456.

23 S. Kattel, P. Atanassov and B. Kiefer, *Phys. Chem. Chem. Phys.*, 2014, **16**, 13800–13806.

24 S. Kattel and G. Wang, *J. Mater. Chem. A*, 2013, **1**, 10790–10797.

25 F. Rusydi, M. K. Agusta, A. G. Saputro and H. Kasai, *J. Phys. Soc. Jpn.*, 2012, **81**, 124301.

26 T. Ikeda, M. Boero, S.-F. Huang, K. Terakura, M. Oshima and J.-I. Ozaki, *J. Phys. Chem. C*, 2008, **112**, 14706–14709.

27 X. Wang, Z. Hou, T. Ikeda, S.-F. Huang, K. Terakura, M. Boero, M. Oshima, M.-A. Kakimoto and S. Miyata, *Phys. Rev. B: Condens. Matter Mater. Phys.*, 2011, **84**, 245434.

28 X. Bao, X. Nie, D. Deak, E. Biddinger, W. Luo, A. Asthagiri, U. Ozkan and C. Hadad, *Top. Catal.*, 2013, **56**, 1623–1633.

29 H. Kim, K. Lee, S. I. Woo and Y. Jung, *Phys. Chem. Chem. Phys.*, 2011, **13**, 17505–17510.

30 F. Studt, *Catal. Lett.*, 2013, **143**, 58–60.

31 J. Dai and J. Yuan, *Phys. Rev. B: Condens. Matter Mater. Phys.*, 2010, **81**, 165414.

32 J. Zhang, Z. Wang and Z. Zhu, *J. Mol. Model.*, 2013, **19**, 5515–5521.

33 M. Li, L. Zhang, Q. Xu, J. Niu and Z. Xia, *J. Catal.*, 2014, **314**, 66–72.

34 L. Zhang and Z. Xia, *J. Phys. Chem. C*, 2011, **115**, 11170–11176.

35 K. A. Kurak and A. B. Anderson, *J. Phys. Chem. C*, 2009, **113**, 6730–6734.

36 R. A. Sidik, A. B. Anderson, N. P. Subramanian, S. P. Kumaraguru and B. N. Popov, *J. Phys. Chem. B*, 2006, **110**, 1787–1793.

37 E. Vayner and A. B. Anderson, *J. Phys. Chem. C*, 2007, **111**, 9330–9336.

38 M. Jain, S.-h. Chou and A. Siedle, *J. Phys. Chem. B*, 2006, **110**, 4179–4185.

39 L. Qin, L. Wang, X. Yang, R. Ding, Z. Zheng, X. Chen and B. Lv, *J. Catal.*, 2018, **359**, 242–250.

40 A. G. Saputro and H. Kasai, *Phys. Chem. Chem. Phys.*, 2015, **17**, 3059–3071.

41 A. K. Fajrial, A. G. Saputro, M. K. Agusta, F. Rusydi, Nugraha and H. K. Dipojono, *Phys. Chem. Chem. Phys.*, 2017, **19**, 23497–23504.

42 E. F. Holby, G. Wu, P. Zelenay and C. D. Taylor, *J. Phys. Chem. C*, 2014, **118**, 14388–14393.

43 G. Zhao, L. Shi, J. Xu, X. Yan and T. Zhao, *Int. J. Hydrogen Energy*, 2018, **43**, 1470–1478.

44 M. D. Esrafili and P. Mousavian, *Appl. Surf. Sci.*, 2018, **440**, 580–585.

45 N. Yang, X. Zheng, L. Li, J. Li and Z. Wei, *J. Phys. Chem. C*, 2017, **121**, 19321–19328.

46 M. D. Bhatt, G. Lee and J. S. Lee, *J. Phys. Chem. C*, 2016, **120**, 26435–26441.

47 E. Gracia-Espino, *J. Phys. Chem. C*, 2016, **120**, 27849–27857.

48 F. He, K. Li, G. Xie, Y. Wang, M. Jiao, H. Tang and Z. Wu, *Phys. Chem. Chem. Phys.*, 2016, **18**, 12675–12681.

49 X. Bai, E. Zhao, K. Li, Y. Wang, M. Jiao, F. He, X. Sun, H. Sun and Z. Wu, *Carbon*, 2016, **105**, 214–223.

50 X. Zhang, Z. Lu, Z. Fu, Y. Tang, D. Ma and Z. Yang, *J. Power Sources*, 2015, **276**, 222–229.

51 R. Li, Z. Wei and X. Gou, *ACS Catal.*, 2015, **5**, 4133–4142.

52 U. B. Nasini, V. Gopal Bairi, S. Kumar Ramasahayam, S. E. Bourdo, T. Viswanathan and A. U. Shaikh, *ChemElectroChem*, 2014, **1**, 573–579.

53 H. Jiang, Y. Zhu, Q. Feng, Y. Su, X. Yang and C. Li, *Chem. – Eur. J.*, 2014, **20**, 3106–3112.

54 J. P. Paraknowitsch, Y. Zhang, B. Wienert and A. Thomas, *Chem. Commun.*, 2013, **49**, 1208–1210.

55 M. Kaukonen, A. Krasheninnikov, E. Kauppinen and R. Nieminen, *ACS Catal.*, 2013, **3**, 159–165.

56 C. H. Choi, S. H. Park and S. I. Woo, *J. Mater. Chem.*, 2012, **22**, 12107–12115.

57 C. H. Choi, S. H. Park and S. I. Woo, *ACS Nano*, 2012, **6**, 7084–7091.

58 D. Yu, Y. Xue and L. Dai, *J. Phys. Chem. Lett.*, 2012, **3**, 2863–2870.

59 Y. Hu, J. Zhu, Q. Lv, C. Liu, Q. Li and W. Xing, *Electrochim. Acta*, 2015, **155**, 335–340.

60 X.-D. Yang, Y. Zheng, J. Yang, W. Shi, J.-H. Zhong, C. Zhang, X. Zhang, Y.-H. Hong, X.-X. Peng, Z.-Y. Zhou and S.-G. Sun, *ACS Catal.*, 2017, **7**, 139–145.

61 A. Zitolo, V. Goellner, V. Armel, M.-T. Sougrati, T. Mineva, L. Stievano, E. Fonda and F. Jaouen, *Nat. Mater.*, 2015, **14**, 937–942.

62 U. I. Kramm, I. Herrmann-Geppert, J. Behrends, K. Lips, S. Fiechter and P. Bogdanoff, *J. Am. Chem. Soc.*, 2016, **138**, 635–640.

63 A. K. Fajrial, M. F. Abdulkarim, A. G. Saputro, M. K. Agusta and H. K. Dipojono, *Procedia Eng.*, 2017, **170**, 131–135.

64 P. Hohenberg and W. Kohn, *Phys. Rev.*, 1964, **136**, B864–B871.

65 W. Kohn and L. J. Sham, *Phys. Rev.*, 1965, **140**, A1133–A1138.

66 P. Giannozzi, S. Baroni, N. Bonini, M. Calandra, R. Car, C. Cavazzoni, D. Ceresoli, G. L. Chiarotti, M. Cococcioni, I. Dabo, A. D. Corso, S. de Gironcoli, S. Fabris, G. Fratesi, R. Gebauer, U. Gerstmann, C. Gougoussis, A. Kokalj, M. Lazzeri, L. Martin-Samos, N. Marzari, F. Mauri, R. Mazzarello, S. Paolini, A. Pasquarello, L. Paulatto, C. Sbraccia, S. Scandolo, G. Sclauzero, A. P. Seitsonen, A. Smogunov, P. Umari and R. M. Wentzcovitch, *J. Phys.: Condens. Matter*, 2009, **21**, 395502.

67 J. P. Perdew, K. Burke and M. Ernzerhof, *Phys. Rev. Lett.*, 1996, **77**, 3865–3868.

68 D. Vanderbilt, *Phys. Rev. B: Condens. Matter Mater. Phys.*, 1990, **41**, 7892–7895.

69 S. Grimme, *J. Comput. Chem.*, 2006, **27**, 1787–1799.

70 S. R. Bahn and K. W. Jacobsen, *Comput. Sci. Eng.*, 2002, **4**, 56–66.

71 G. Henkelman, B. P. Uberuaga and H. Jansson, *J. Chem. Phys.*, 2000, **113**, 9901–9904.

72 J. K. Nörskov, J. Rossmeisl, A. Logadottir, L. Lindqvist, J. R. Kitchin, T. Bligaard and H. Jònsson, *J. Phys. Chem. B*, 2004, **108**, 17886–17892.

73 C. E. Szakacs, M. Lefevre, U. I. Kramm, J.-P. Dodelet and F. Vidal, *Phys. Chem. Chem. Phys.*, 2014, **16**, 13654–13661.

74 W.-J. Jiang, L. Gu, L. Li, Y. Zhang, X. Zhang, L.-J. Zhang, J.-Q. Wang, J.-S. Hu, Z. Wei and L.-J. Wan, *J. Am. Chem. Soc.*, 2016, **138**, 3570–3578.

75 B. Zheng, J. Wang, F.-B. Wang and X.-H. Xia, *Electrochem. Commun.*, 2013, **28**, 24–26.

76 J. Tai, J. Hu, Z. Chen and H. Lu, *RSC Adv.*, 2014, **4**, 61437–61443.

77 L. Qu, Y. Liu, J.-B. Baek and L. Dai, *ACS Nano*, 2010, **4**, 1321–1326.

78 N. D. M. Hine, K. Frensch, W. M. C. Foulkes and M. W. Finnis, *Phys. Rev. B: Condens. Matter Mater. Phys.*, 2009, **79**, 024112.

79 S. Kirklin, J. E. Saal, B. Meredig, A. Thompson, J. W. Doak, M. Aykol, S. Ruhl and C. Wolverton, *npj Comput. Mater.*, 2015, **1**, 15010.

80 S. Gupta, S. Zhao, O. Ogoke, Y. Lin, H. Xu and G. Wu, *ChemSusChem*, 2017, **10**, 774–785.

81 R. Hultgren, N. Gingrich and B. Warren, *J. Chem. Phys.*, 1935, **3**, 351–355.

82 R. Wyckoff, *Crystal structures, rocksalt structure*, Interscience Publishers, New York, 1963, pp. 85–237.

83 L. Cartz, S. Srinivasa, R. Riedner, J. Jorgensen and T. Worlton, *J. Chem. Phys.*, 1979, **71**, 1718–1721.

84 S. Li, W. Xu, P. Cheng, J. Luo, D. Zhou, J. Li, R. Li and D. Yuan, *Synth. Met.*, 2017, **223**, 137–144.

85 M. Tsuda, W. A. Dino, H. Nakanishi and H. Kasai, *Chem. Phys. Lett.*, 2005, **402**, 71–74.

86 M. Tsuda, E. Sy Dy and H. Kasai, *J. Chem. Phys.*, 2005, **122**, 244719.

87 T. Q. Nguyen, M. C. S. Escaño, N. Shimoji, H. Nakanishi and H. Kasai, *Phys. Rev. B: Condens. Matter Mater. Phys.*, 2008, **77**, 1–7.

88 W. Liang, J. Chen, Y. Liu and S. Chen, *ACS Catal.*, 2014, **4**, 4170–4177.

89 M. Aoki, H. Uchida and M. Watanabe, *Electrochem. Commun.*, 2006, **8**, 1509–1513.

90 J. Qiao, M. Saito, K. Hayamizu and T. Okada, *J. Electrochem. Soc.*, 2006, **153**, A967–A974.

91 D. E. Curtin, R. D. Lousenberg, T. J. Henry, P. C. Tangeman and M. E. Tisack, *J. Power Sources*, 2004, **131**, 41–48.

92 A. G. Saputro, A. K. Fajrial, M. K. Agusta and H. K. Dipojono, *J. Phys.: Conf. Ser.*, 2019, **1204**, 012119.

93 F. Mehmood, R. Pachter, W. Lu and J. J. Boeckl, *J. Phys. Chem. C*, 2013, **117**, 10366–10374.

94 Z. Lu, S. Li, C. Liu, C. He, X. Yang, D. Ma, G. Xu and Z. Yang, *RSC Adv.*, 2017, **7**, 20398–20405.

95 Z. Ao, J. Yang, S. Li and Q. Jiang, *Chem. Phys. Lett.*, 2008, **461**, 276–279.

96 M. Chi and Y.-P. Zhao, *Comput. Mater. Sci.*, 2009, **46**, 1085–1090.

97 Y. Chen, B. Gao, J.-X. Zhao, Q.-H. Cai and H.-G. Fu, *J. Mol. Model.*, 2012, **18**, 2043–2054.

98 Y. Chen, X.-c. Yang, Y.-j. Liu, J.-x. Zhao, Q.-h. Cai and X.-z. Wang, *J. Mol. Graphics Modell.*, 2013, **39**, 126–132.